

Self-consistent models of our Galaxy

James Binney^{1*} and Eugene Vasiliev²

¹*Rudolf Peierls Centre for Theoretical Physics, Clarendon Laboratory, Oxford, OX1 3PU, UK*

²*Institute of Astronomy, Madingley Road, Cambridge CB3 0HA*

9 June 2022

ABSTRACT

A new class of models of stellar discs is introduced and used to build a self-consistent model of our Galaxy. The model is defined by the parameters that specify the action-based distribution functions (DFs) $f(\mathbf{J})$ of four stellar discs (three thin-disc age cohorts and a thick disc), spheroidal bulge and spheroidal stellar and dark haloes. From these DFs plus a specified distribution of gas, we solve for the densities of stars and dark matter and the potential they generate. The principal observational constraints are the kinematics of stars with Gaia RVS data and the density of stars in the column above the Sun. The model predicts the density and kinematics of stars and dark matter throughout the Galaxy. We determine the structure of the dark halo prior to the infall of baryons. A simple extension of the DFs of stellar components to include chemistry allows the model to reproduce the way the Galaxy’s chemistry is observed to vary in the (R, z) plane. Surprisingly, the data indicate that high- α stars are confined to orbits with $J_z \gtrsim 50 \text{ kpc km s}^{-1}$. The code used to create the model is available on GITHUB.

Key words: Galaxy: kinematics and dynamics – galaxies: kinematics and dynamics – methods: numerical

1 INTRODUCTION

The volume and quality of the observational data that are available for our Galaxy have increased spectacularly over the last decade. The spectra of millions of stars have been taken from the ground, while ESA’s satellite Gaia has been tracking the motion across the sky of over a billion stars, deriving for them photometry of unprecedented precision, and measuring the line-of-sight velocities of millions of the brighter stars. The astrophysical community now faces the challenge of synthesising these data into a coherent physical picture of how our archetypal Galaxy is structured, how it functions as a machine, and how it arrived at this state.

While ideally one would exploit the data for all the $> 10^9$ stars that Gaia has been tracking, many studies have focused on the $\sim 7 \times 10^6$ stars for which Gaia has measured line-of-sight velocities (Helmi et al. 2018; Antoja et al. 2018; Hunt et al. 2019; Sellwood et al. 2019; Trick et al. 2019; Gaia Collaboration et al. 2021). We shall see that this subsample of the Gaia data is large enough for Poisson noise to be insignificant, and it is relatively easy to model because when the line-of-sight velocities are missing, one has to marginalise over them, which is computationally expensive (e.g. Li & Binney 2022a). The potential strengths of the much larger sample of all Gaia stars are (i) that it extends to much fainter magnitudes, and thus covers a more

significant slice of our Galaxy, and (ii) that it should be possible to determine its selection function. Sadly, however, at the current time it is hard to determine the probability that the data for a star of given magnitude, and sky-coordinates will pass a given quality threshold (Boubert & Everall 2020; Everall et al. 2021), and impossible to predict the apparent magnitudes of distant stars of given absolute magnitudes on account of the poorly known distribution of dust in the Galaxy (e.g. Li & Binney 2022b). These problems can be to a large extent side-stepped by modelling the distribution of velocities at given locations because the probability of a star entering Gaia’s radial-velocity sample (RVS) is independent of its velocity. In this paper we fit to Gaia RVS data self-consistent, axisymmetric models of our Galaxy that are defined by distribution functions (DFs) that are analytic functions of the action integrals J_i .

Most previous fits of kinematic data have adopted a simple functional form for the density of dark matter (DM) (Robin et al. 2003; Binney 2010; Bovy & Rix 2013; Piffl et al. 2014). This procedure is unsatisfactory both because DM will actually respond in a non-trivial way to the gravitational field of the stars, which is strongly flattened, and because it yields no information regarding the velocity distribution of local DM, which is important from the perspective of experiments to detect DM on Earth. Here our approach is basically that pioneered by Piffl et al. (2015) in which a distribution function (DF) $f(\mathbf{J})$ that depends on the action integrals J_i is assigned to both DM and various stellar pop-

* E-mail: binney@physics.ox.ac.uk

ulations, and then the gravitational field that stars and DM jointly generate is determined iteratively.

Whereas Piffl et al. (2015) simply computed one not very satisfactory model, Binney & Piffl (2015) and Cole & Binney (2017) searched the space of candidate DFs for ones that were consistent with data. The data they employed were rather heterogeneous: astrometry of some stellar masers (Reid & Brunthaler 2004), terminal velocities of neutral hydrogen and carbon monoxide (Malhotra 1995), star counts from the Sloan Digital Sky Survey (Abazajian et al. 2003) and the kinematics of giant stars measured by the Radial Velocity Experiment (RAVE; Steinmetz & et al. 2006). The heterogeneity of the data combined with sub-optimal numerical methods made the search for an acceptable model computationally expensive.

Here we use the AGAMA software library (Vasiliev 2019) to show that the data for stars with Gaia line-of-sight velocities is so extensive that they strongly constrain DFs for stars and DM on their own. We do this by constructing fully self-consistent dynamical models of the Galaxy. These models are, for the first time, completely specified only by their DF: all other quantities – their density distributions, gravitational potential and kinematics – follow from the DF. In Section 2 we describe a new family of DFs for stellar discs, and in Section 3 we describe the DFs we use to represent the bulge and the dark and stellar haloes. In Section 4 we compare one of our models with Gaia kinematics and a variety of older data sources. This comparison confirms that the Galaxy’s circular speed declines outwards at the solar radius and yields values for the local densities of stars and dark matter. We infer the structure of the dark halo before the baryons fell in under both the assumption of adiabatic invariance and the assumption that the dark halo originally had a central density cusp that was eliminated by baryons upscattering dark-matter particles. In Section 4.6 we show that reasonable hypotheses regarding the chemical compositions of the model’s stellar components provides a good fit to the distribution of stars in the $([\alpha/\text{Fe}], [\text{Fe}/\text{H}])$ plane at various locations (R, z) that were reported by Hayden et al. (2015).

2 A NEW FAMILY OF DFS FOR DISCS

Binney (2012), Bovy & Rix (2013), Piffl et al. (2014) and several others modelled the Galaxy’s discs with the quasi-isothermal DF that was introduced by Binney (2010) and modified to its current form by Binney & McMillan (2011). This DF was introduced in the context of solar-neighbourhood kinematics using an analytic model of the Galactic potential Φ . Weaknesses in this DF emerged when Piffl et al. (2015), Binney & Piffl (2015) and Cole & Binney (2017) used it while computing the self-consistently generated potential. They employed ad-hoc work-arounds for these problems, but it is now time to address these problems clinically and resolve them in a satisfying way. Our discussion extends that in Section 4.4 of Vasiliev (2019).

The root problem with the quasi-isothermal DF is that it references the circular radius $R_c(J_\phi)$ and the radial and vertical epicycle frequencies $\kappa(J_\phi)$ and $\nu(J_\phi)$. The way these quantities vary with J_ϕ depends on the potential, so when they appear in the DF, the latter is no longer a function of

Table 1. Default parameter values of the DF that a disc component. Actions are given in kpc km s^{-1} .

J_{r0}	J_{z0}	$J_{\phi0}$	p_r	p_z	J_{v0}	J_{d0}
18	6	700	0.5	0.5	200	150

the actions alone. This dependence of the DF on Φ endangers the convergence of the algorithm Binney (2014) introduced for finding the potential. The problem can be evaded by using the functions $R_c(J_\phi)$, etc., associated with a fixed but suitable potential instead of the real potential, but this fix is inelegant and means that a model is not uniquely specified by a set of DFs.

Another problem with the quasi-isothermal DF is that it ceases to make sense physically for orbits that are highly eccentric or strongly inclined to the plane. Therefore we now write down an extension of the Exponential DF defined by Vasiliev (2019) that does not reference R_d , κ or ν and is physically reasonable throughout action space

Let $J_{\phi0}$, J_{v0} and J_{d0} be three fixed actions, the first much larger than the other two. Then we define

$$J_v \equiv |J_\phi| + J_{v0} \quad \text{and} \quad J_d \equiv |J_\phi| + J_{d0} \quad (1)$$

and take the DF of a disc component to be

$$f(\mathbf{J}) = f_\phi(J_\phi) f_r(J_\phi, J_r) f_z(J_\phi, J_z), \quad (2)$$

where the functions f_r and f_z have the common form

$$f_i(J_\phi, J_i) = \left(\frac{J_v}{J_{\phi0}} \right)^{p_i} \frac{1}{J_{i0}} \exp \left[- \left(\frac{J_v}{J_{\phi0}} \right)^{p_i} \frac{J_i}{J_{i0}} \right] \quad (i = r, z). \quad (3)$$

Here the prefactor ensures that $1 \simeq \int_0^\infty dJ_i f_i$. The factor $(J_v/J_{\phi0})^{p_i}$ in the exponential controls the radial gradient in the velocity dispersion σ_i .

The function $f_\phi(J_\phi)$ in equation (2) determines the radial structure of the disc. We adopt

$$f_\phi(J_\phi) \equiv \begin{cases} 0 & \text{when } J_\phi < 0 \\ \frac{M}{(2\pi)^3} \frac{J_\phi}{J_{\phi0}^2} e^{-J_d/J_{\phi0}} & \text{if } J_\phi > 0. \end{cases} \quad (4)$$

The vanishing of f for $J_\phi < 0$ sets this DF apart from several earlier DFs for discs, including that of Vasiliev (2019), who proposed using for $J_\phi < 0$ the same formula as for $J_\phi > 0$ multiplied by an additional factor

$$\exp \left(\frac{J_v J_\phi}{J_{r0}} \right). \quad (5)$$

When the DF at $J_\phi < 0$ is taken to be a multiple of the DF at $J_\phi > 0$ in this way, one is implicitly assuming that there is a retrograde disc like the prograde one but with reduced density. This is not the natural assumption: rather we suppose that any disc stars that are now on retrograde orbits have been scattered onto such orbits after being born on more-or-less eccentric co-rotating orbits. Thus most retrograde stars should be on highly inclined or eccentric orbits and an implicit assumption that the co-rotating disc is shadowed by a counter-rotating counterpart is unnatural. More natural is to deem any counter-rotating stars to belong to a hot component, such as the bulge or the stellar halo. Since the DF should be a continuous function on action space, we arrange for the DF to go to zero as $J_\phi \rightarrow 0+$ by replacing J_d in the first line of equation (21) in Vasiliev (2019) by J_ϕ .

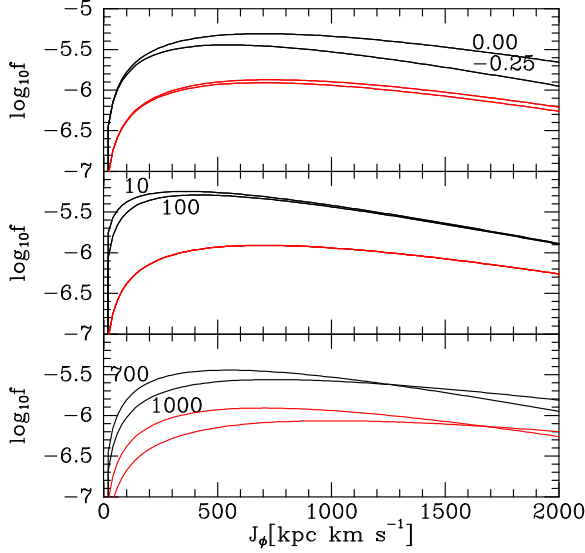


Figure 1. How the parameters $J_{\phi 0}$ (bottom panel), J_v (middle panel) and p_i (top panel) affect the DF. Black curves give values of the disc DF for $J_r = J_z = 0$, while red curves show values for generic actions $(J_r, J_z) = (10, 5) \text{ kpc km s}^{-1}$. In the bottom panel $J_{\phi 0}$ is set to 700 and 1000 kpc km s^{-1} with the other parameters as listed in Table 1. In the middle panel J_v is set to 10 and 100 kpc km s^{-1} with the other parameters as in Table 1. In the top panel $p_r = p_z$ are set to -0.25 and 0 .

Here we present some examples of how the characteristics of a disc component vary with the parameters that specify its DF through equations (1) to (4). Table 1 lists the default values taken by parameters that are not explicitly given in each example.

2.1 How the parameters affect the DF's values

The scale actions J_{r0} and J_{z0} set the scale on which the DF declines as J_r and J_z increase: larger J_{z0} implies larger vertical velocity dispersion σ_z , while increasing J_{r0} increase both σ_R and σ_ϕ . In the bottom panel of Fig. 1 we plot in black f versus J_ϕ with $J_r = J_z = 0$ for two values of $J_{\phi 0}$. Corresponding values for $(J_r, J_z) = (10, 5) \text{ kpc km s}^{-1}$ are plotted in red. $J_{\phi 0}$ sets the scale over which the DF decreases as J_ϕ grows. The steeper the decline, the smaller will be the scale length of the resulting exponential disc, so $J_{\phi 0}$ is a surrogate for R_d .

In the middle panel of Fig. 1, the black and red curves are again for $(J_r, J_z) = (0, 0)$ and $(10, 5) \text{ kpc km s}^{-1}$ but the curves in each colour are now for $J_{v0} = 10$ and $100 \text{ kpc km s}^{-1}$. We see that even a ten-fold increase in J_{v0} has only a small effect on the value of the DF, so J_{v0} is not an important parameter: its role is to prevent the velocity dispersions diverging (for $p_i > 0$) or vanishing (if $p_i < 0$) at the centre.

The top panel of Fig. 1 shows how the DF varies with J_ϕ for two pairs of values, $(p_r, p_z) = (0, 0)$ and $(-0.25, -0.25)$, of the power-law exponents p_r and p_z . Reducing the p_i reduces the difference between the slopes of the black curves for circular orbits ($J_r = J_z = 0$) and the red curves for non-zero eccentricity and inclination. A large separation between the red and black curves implies a DF that falls rapidly with

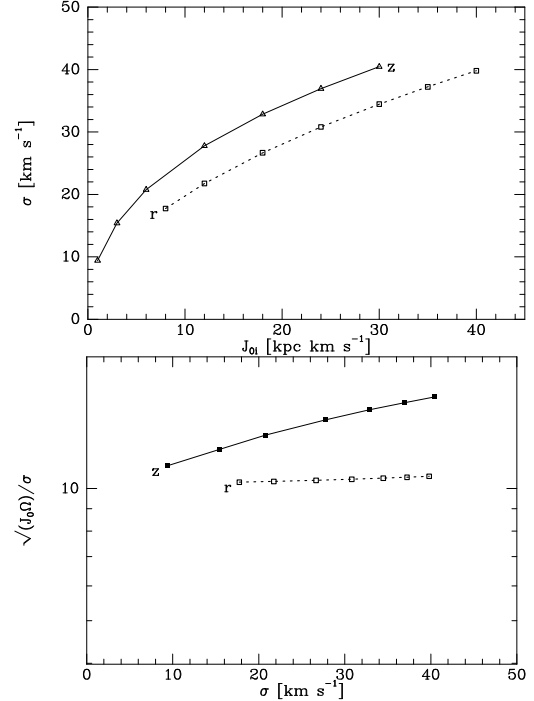


Figure 2. Upper panel: the radial (full line) and vertical (dashed line) velocity dispersions at $R_0 = 8.27 \text{ kpc}$ induced in a disc by the characteristic action J_{0i} ($i = r, z$) that appears in equation (3). Lower panel: the relationship between the velocity dispersion (radial or vertical) in a disc and the square root of the product of the characteristic action J_{i0} in the DF and the mean orbital frequency $\langle \Omega_i \rangle$.

increasing eccentricity/inclination and thus small values of the velocity dispersions σ_R and σ_z . Hence reducing the p_i increases the velocity dispersions at large radii relative to their values at small radii.

2.2 Observational significance of parameters

The real-space structure of a component depends on the gravitational potential in which it resides. In general that potential depends on all the model's components, so it will change with any component's parameters. Here in the interests of clarity we fix the potential, choosing the potential of a model that provides a good fit to observational data. Thus we adopt a very realistic potential and explore how the structure of a single component depends on the parameters in its DF.

2.2.1 Roles of the characteristic actions $J_{\phi 0}$, J_{r0} and J_{z0}

The most important parameters are the three characteristic actions J_{i0} , where $i = r, z, \phi$. While $J_{\phi 0}$ sets the component's scale length, J_{r0} and J_{z0} set the in-plane and vertical dispersions, respectively. By setting these dispersions through J_{r0} and J_{z0} , we simultaneously determine a component's vertical density profile and asymmetric drift through standard dynamics.

The upper panel of Fig. 2 shows the relationship between J_{r0} and J_{z0} and the velocity dispersions in the plane

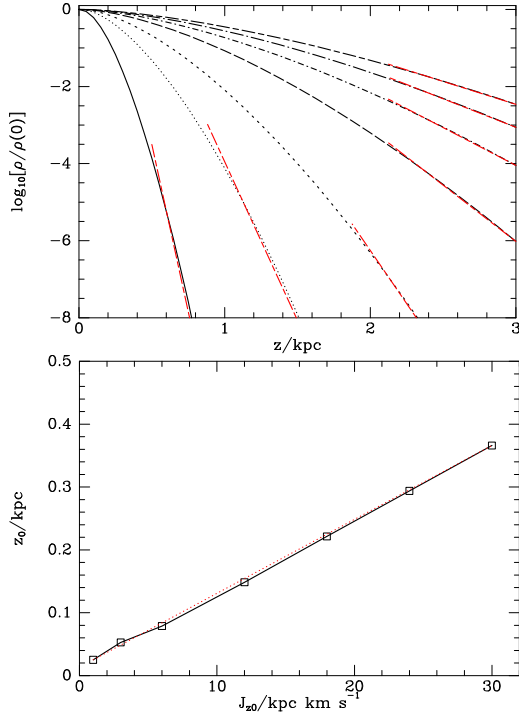


Figure 3. Upper panel: the vertical density profiles at $R_0 = 8.27 \text{ kpc}$ in disc components with $J_{z0} = 1, 3, 6, 12, 18, 24$ and 30 kpc km s^{-1} . The red curves are perfect exponentials fitted to the last eight points. Lower panel: asymptotic scale height as a function of J_{z0} . The red dotted line has slope $0.012 \text{ km}^{-1} \text{ s}$

at $R_0 = 8.27 \text{ kpc}$. The lower panel shows that both dispersion satisfy quite accurately the relationship

$$\sigma \simeq \sqrt{\langle \Omega_i \rangle J_{i0}}, \quad (6)$$

where $\langle \Omega_i \rangle$ is the mean value of Ω_i of the given disc's stars sampled at $(R, z) = (R_0, 0)$. A relationship of this type is suggested by the fact that $J_z d\theta_z = v_z dz + dh$, where $h(\mathbf{x}, \mathbf{v})$ is some function on phase space: when we divide both sides by dt and average along an orbit $\langle dh/dt \rangle = 0$, so when we further average over orbits we expect to find $J_z \langle \Omega_z \rangle = \langle v_z^2 \rangle$. This argument indicates that in the case $p_i = 0$, when the exponentials in the DF make $\langle J_i \rangle$ the same throughout action space, velocity dispersions should fall in parallel with frequencies. In particular we expect σ_z to fall with increasing distance from the plane, and both σ_R and σ_z to fall roughly as $1/R$ with distance from the Galactic centre.

The upper panel of Fig. 3 shows the vertical density profiles of the components plotted in Fig. 2. The profiles steepen rapidly from zero in the plane to a nearly perfect exponentials once the density has fallen to less than a tenth of its central values. The lower panel of Fig. 3 plots the resulting asymptotic scale-height against J_{z0} . The relationship is almost exactly linear:

$$\frac{z_0}{\text{kpc}} \simeq 0.012 \frac{J_{z0}}{\text{kpc km s}^{-1}}. \quad (7)$$

Fig. 4 shows how the vertical velocity dispersion in a disc component varies with height above the plane. The dispersion falls slowly as expected from the argument above relating σ_z to the mean frequency Ω_z , while the density de-

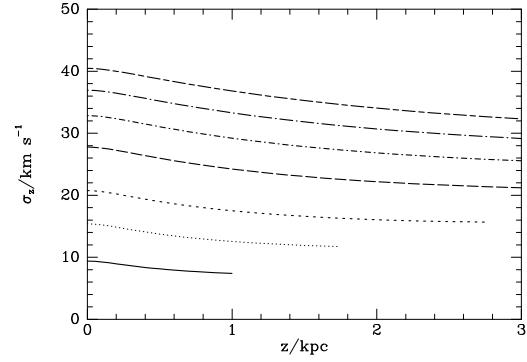


Figure 4. The variation at $R_0 = 8.27 \text{ kpc}$ with z of the vertical velocity dispersion of disc components with $J_{z0} = 1, 3, 6, 12, 18, 24$ and 30 kpc km s^{-1} . The curves are terminated when $\rho(z)/\rho(0)$ falls to 10^{-10} .

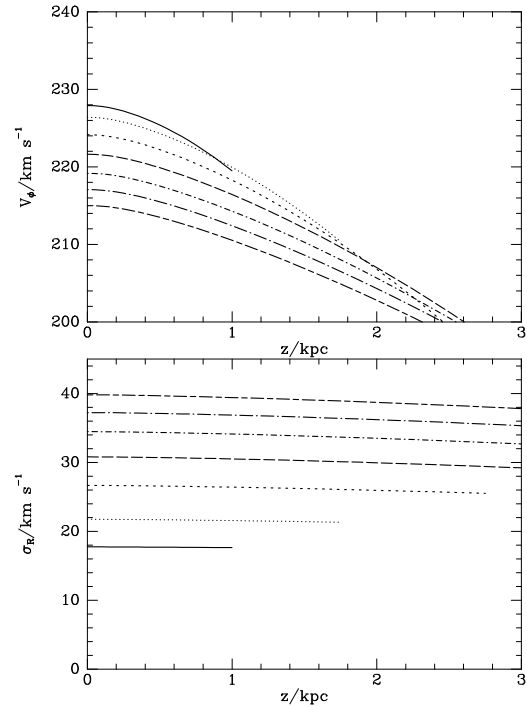


Figure 5. The variation at $R_0 = 8.27 \text{ kpc}$ with z of $\langle V_\phi \rangle$ (upper panel) and σ_R (lower panel) in increasingly hot disc components: from top to bottom in the upper panel the characteristic actions are $(J_{r0}, J_{z0}) = (8, 1), (12, 3), (18, 6), (24, 12), (30, 18), (35, 24)$ and $(40, 30) \text{ kpc km s}^{-1}$. The curves are terminated when $\rho(z)/\rho(0)$ falls to 10^{-10} .

clines by orders of magnitude. The decline in σ_z is steepest near the mid-plane.

Fig. 5 shows the mean rotation speed (upper panel) and the radial velocity dispersion (lower panel) in a disc component at $R_0 = 8.27 \text{ kpc}$ as functions of height. The radial velocity dispersions are to high precision independent of height. The thinnest components have, by construction, the smallest dispersions, so at $z = 0$ they rotate fastest – they show the least asymmetric drift. In every component $\langle V_\phi \rangle$ falls appreciably with height.

The upper panel of Fig. 6 shows the radial density profiles of the disc components with $(J_{r0}, J_{z0}) = (8, 1), (18, 6)$

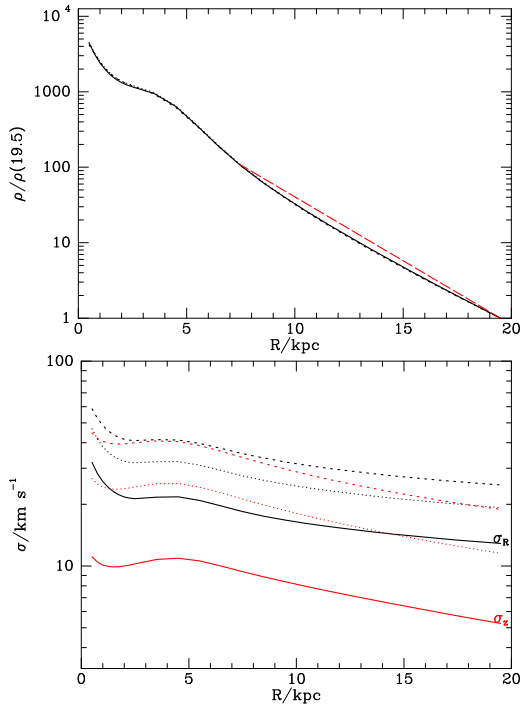


Figure 6. Upper panel: the variation with R of the density at $z = 0$ of disc components with $(J_{r0}, J_{z0}) = (8, 1), (18, 6)$ and $(30, 18) \text{ kpc km s}^{-1}$. The dashed red line shows an exponential decline with scale-length 2.72 kpc . Lower panel: the mid-plane velocity dispersions of these components in the radial (black) and vertical (red) directions.

and $(30, 18) \text{ kpc km s}^{-1}$. Beyond R_0 these profiles are quite accurately exponential with the common scale length $R_d = 2.72 \text{ kpc}$ that is indicated by the red dashed line. This scale-length is set by the value $J_{\phi 0} = 700 \text{ kpc km s}^{-1}$ assigned to all components. Interior to R_0 the profiles acquire structure from the bulge via the self-consistently generated potential, as will be described below. Despite this structure, the profiles approximate exponentials at all R .

The lower panel of Fig. 6 shows the dependence on radius of the velocity dispersions of these components in the radial (black) and vertical (red) directions. The ratio σ_z/σ_R increases rapidly with disc thickness, approaching unity for the hottest disc plotted [which has $(J_{r0}, J_{z0}) = (35, 24) \text{ kpc km s}^{-1}$]. This result is a natural consequence of the decision to have J_{r0} span a smaller range ($8 - 40 \text{ kpc km s}^{-1}$) than J_{z0} ($1 - 30 \text{ kpc km s}^{-1}$). In the thinnest disc (full curves) the vertical dispersion falls almost exponentially with R , while the radial dispersion falls more slowly. This result reflects the fact that Ω_z is much more sensitive than Ω_r to the contribution of the disc to the overall gravitational field: around R_0 the density of the disc that generates the gravitational field used for these figures is declining nearly exponentially with R .

2.2.2 Role of the exponents p_r and p_z

The exponents p_r and p_z that occur in equation (3) moderate the rates at which the σ_R and σ_z decrease outwards. The results plotted above are for $p_i = 0$. We will find that

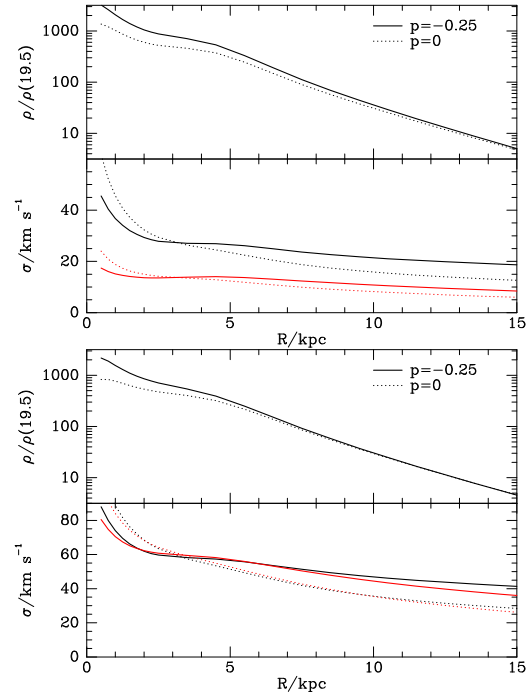


Figure 7. The real-space consequences of changing the exponents p_i in discs that are cold (top) and hot (bottom). The cold disc has $(J_{r0}, J_{z0}) = (8, 1) \text{ kpc km s}^{-1}$, while the hot disc has $(J_{r0}, J_{z0}) = (30, 40) \text{ kpc km s}^{-1}$ and in all cases $p_r = p_z$. Full curves are for $p_i = -0.25$, which yields a slower decline in velocity dispersions with R than the larger value of p_i .

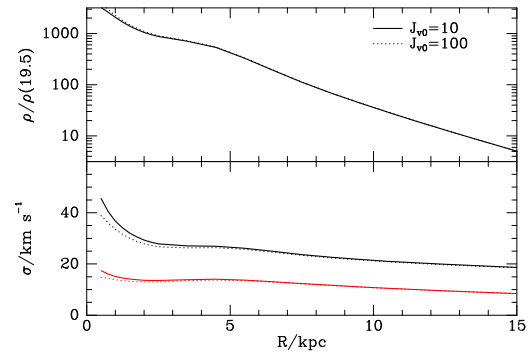


Figure 8. Real-space consequences of increasing the parameter J_{v0} . Full curves are for $J_{v0} = 10 \text{ kpc km s}^{-1}$ and the barely visible dotted curves are for $J_{v0} = 100 \text{ kpc km s}^{-1}$. These results are for a cold disc $(J_{r0}, J_{z0}) = (8, 1) \text{ kpc km s}^{-1}$; increasing J_{v0} has an even smaller impact on a hot disc.

data for our Galaxy requires slightly negative values of p_i , which cause σ_R and σ_z to decrease outwards more slowly.

In Fig. 7 we show the mid-plane density and velocity dispersions for $p_i = -0.25$ (full curves) and $p_i = 0$ in the case of a cold disc and a hot disc (lower pair of panels). Larger values of p_i correspond to steeper outward gradients of the dispersions, as expected.

2.2.3 Role of the characteristic action J_{v0}

Fig. 8 shows the effect on a cold disc of increasing the characteristic action J_{v0} from 10 to $100 \text{ kpc km s}^{-1}$. This pa-

parameter is active only for non-zero p_i , so Fig. 8 compares profiles for a disc with $p_i = -0.5$. As expected, J_{v0} has a perceptible effect only near the centre and in the sense that larger values lower the central velocity dispersions, and by hydrostatic balance, correspondingly increase the central mid-plane density. However, the effect on the plotted cold disc of even ten-fold decrease in J_{v0} is extremely small. The effect is no larger in the case of a hot disc.

3 HALO DFS

To build a self-consistent model Galaxy we require DFs for at least two hot components: the dark halo and the bulge / stellar halo. On account of the Galactic bar, a satisfactory model of the bulge would be non-axisymmetric so cannot be provided with our technology and we are obliged to model the bulge as an axisymmetric structure. Since few bulge stars reach the volume around the Sun in which the Gaia data are most precise, and the non-axisymmetric components of the bulge's gravitational field decay strongly with increasing Galactocentric radius, we anticipate obtaining useful results even with a completely axisymmetric model.

For all three hot components of our Galaxy we employ a modified double power-law DF that is related to, but different from, those introduced by Posti et al. (2015) – hereafter P15. Our modifications of the P15 proposal are two-fold. First the phase-space density at the origin of action space is made finite by the mechanism introduced by Cole & Binney (2017). Second, the linear combination of actions $h = J_r + \eta_z J_z + \eta_\phi |J_\phi|$ that forms the basis of the P15 proposal is replaced by a more complex function of the actions. A full explanation of this replacement lies beyond the scope of this paper and will be presented elsewhere (Binney 2022) but it addresses a weakness of the P15 proposal that was mentioned already by Binney & Piffl (2015), namely unphysical behaviour of velocity distributions at small $|V_\phi|$.

The P15 halo DF is

$$f = \frac{M}{(2\pi J_0)^3} \frac{(1 + J_0/h)^\alpha}{(1 + g/J_0)^\beta} \exp(-[g/J_{\text{cut}}]^\delta). \quad (8)$$

Instead of the linear combinations $g(\mathbf{J})$ and $h(\mathbf{J})$, we use

$$g(\mathbf{J}) = h(\mathbf{J}) = J_r e^{-\beta \sin(c\pi/2)} + \frac{1}{2}(1 + c\xi) e^{\beta \sin(c\pi/2)} \mathcal{L}. \quad (9)$$

Here

$$c \equiv \frac{L}{L + J_r} \quad (10)$$

with $L \equiv J_z + |J_\phi|$ is a measure of an orbit's circularity and

$$\mathcal{L}(J_z, J_\phi) \equiv aL_z + b \frac{J_z |J_\phi|}{L} + |J_\phi| \quad (11)$$

is a generalisation of the total angular momentum. The constants a and b in the definition of \mathcal{L} are chosen such that $\partial \mathcal{L} / \partial V_\phi$ vanishes as $V_\phi \rightarrow 0$. Specifically

$$a = \frac{1}{2}(k + 1) \text{ and } b = \frac{1}{2}(k - 1), \quad (12)$$

where k is a number greater or equal to unity. We allow k to depend on energy by writing

$$k(\xi) = (1 - \xi)F_{\text{in}} + \xi F_{\text{out}} \quad (13)$$

where F_{in} and F_{out} are constants and ξ is a dimensionless surrogate for energy that increases from zero at the origin

Table 2. The boundaries (kpc) of the bins in the $(R, |z|)$ plane used to construct velocity histograms from Gaia data and models.

$R - R_0$	-3	-1.5	-0.5	0.5	1.5	3		
$ z $	0	0.1	0.2	0.35	0.5	1	1.75	3

of phase space to unity for marginally bound orbits through the formula

$$\xi \equiv \frac{j_t^\alpha}{j_t^\alpha + 1} \quad (14)$$

where $\alpha \simeq 0.6$ and

$$j_t \equiv \frac{1.5J_r + L}{L_0}, \quad (15)$$

where $L_0 \simeq 6J_0$ is a scale action.

When $F_{\text{in}} = F_{\text{out}} = 1$, $\mathcal{L} = L$ and in a spherical potential the distributions of V_θ and V_ϕ are identical. If α and L_0 are then set to the values suggested above, the velocity distribution becomes isotropic when $\beta = 0$ and radially biased when $\beta > 0$. To flatten the component in a spherical potential, one sets F_{in} and F_{out} above unity. If the potential is flattened, setting $\beta = 0$, and F_{in} and F_{out} to the ratio ν/Ω of vertical to azimuthal epicycle frequencies at small and large radii, respectively causes the velocity distribution to be nearly isotropic.

4 MODELS OF OUR GALAXY

In this section we use the DFs for disc components defined above to fit multi-component, self-consistent models to data for stars in the Gaia DR2 release (Gaia Collaboration & Brown 2018) for which the Radial Velocity Spectrometer (RVS) measured line-of-sight velocities (Gaia Collaboration & Katz 2018).

4.1 The data

We used the stellar locations and velocities computed by Schönrich et al. (2019) for the RVS stars. These authors adopted $R_0 = 8.27$ kpc as the distance to the Galactic centre and $(U_0, V_0, W_0) = (11.1, 250, 7.47)$ km s⁻¹ as the Sun's Galactocentric velocity. According to this assumption, the Sun is moving towards the Galactic centre, ahead of the local circular speed $\Theta_0 = 239$ km s⁻¹ and up out of the plane. They determined a distance-dependent selection function of the RVS sample and used the kinematic method of Schönrich et al. (2012) to determine the offset of Gaia DR2 parallaxes. After determining this offset, they obtained moments for the probability distribution of the distance to each star using the Bayesian technique of Schönrich & Aumer (2017).

We restricted the sample to stars with quoted uncertainties $\sigma_\varpi < \varpi/5$ smaller than a fifth of their parallax ϖ . The selection function of the RVS sample is complex (Everall et al. 2021) and a decision was taken not to engage with it in this preliminary work. From this decision it follows that we cannot attach significance to the *number* of stars listed in any spatial bin; only the distribution of these stars in velocity is significant.

We used the data given by Schönrich et al. (2019) to

compute the histograms of Galactocentric velocity components V_R , V_z and V_ϕ for each of 35 spatial bins. These bins are defined by a rectangular grid in the $(R, |z|)$ plane that stretches from $R_0 - 3$ kpc to $R_0 + 3$ kpc and from the plane up to $|z| = 3$ kpc. Table 2 defines this grid.

4.2 Observational uncertainties

We investigated the impact of observational uncertainties on the histograms by drawing a sample from a realistic model using the approximation to the RVS selection function given by Schönrich et al. (2019) and comparing the histograms one obtains from the raw sample and from the sample after the stars have been scattered by the uncertainties in distance, proper motion and line-of-sight velocity. The uncertainties in each observable were averages of the DR2 uncertainties given for stars that lay at essentially the same distance from us – we used 50 equal-width bins in distance out to 3 kpc. We checked the correctness of the code by computing the differences between the observables before and after scattering and showing that the standard deviations of these differences agree with the uncertainties used to scatter the stars.

Errors in velocities will be most important for the most distant stars, so Fig. 9 shows their effect on the most distant bins, looking inward in the lower row of panels and outward in the upper row. The red histograms computed after scattering stars essentially obliterate the black histograms computed before scattering the raw sample. This perhaps surprising result allows us to neglect observational uncertainties even when using DR2 data, and in the following we compare histograms from Gaia with the model’s distribution of velocities at the barycentre of the Gaia stars in each bin. EDR3 data is superior to DR2 data in that its astrometric uncertainties are smaller, so if we upgraded to EDR3 data, more stars would pass our quality cuts so more stars would contribute to each histogram, and observational uncertainties would be even less significant. But given that our data/model comparisons are limited neither by Poisson noise nor by observational uncertainties, we continue to use the DR2 data.

4.3 The models

Our Galaxy models comprise eight components of which seven are defined by DFs and the eighth, the gas disc, is defined as a density distribution that contributes to the total potential. Following Dehnen & Binney (1998) the gas disc has density

$$\rho_g(R) = \frac{\Sigma_0}{4z_0} e^{-R/R_d - R_h/R} \text{sech}^2\left(\frac{z}{2z_0}\right). \quad (16)$$

with $\Sigma_0 = 1.3 \times 10^8 \text{ M}_\odot \text{ kpc}^{-2}$, $R_d = 5$ kpc, $R_h = 5$ kpc and $z_0 = 60$ pc. This gas disc has total mass $1.04 \times 10^{10} \text{ M}_\odot$, and at the solar radius $R_0 = 8.27$ kpc has surface density $\Sigma_g(R_0) = 13.6 \text{ M}_\odot \text{ pc}^{-2}$ and central density $\rho_g(R_0, 0) = 0.057 \text{ M}_\odot \text{ pc}^{-3}$.

We include three spheroidal components – a dark halo, a bulge and a stellar halo – and four disc components – a thick disc and old ($\tau > 6$ Gyr), middle-aged ($6 > \tau > 2$ Gyr), and young components ($\tau < 2$ Gyr) of the thin disc. Each of these discs has a DF of the type defined in Section 2, while

the spheroidal components have DFs of the type defined in Section 3.

4.4 Fitting Gaia data

AGAMA computes the density of each component on an appropriate grid (spherical for the dark halo and cylindrical for the stellar components) using an assumed potential, then it solves Poisson’s equation for the resulting potential and re-determines the density in this new potential. This sequence of potential determinations is quite rapidly convergent. An excellent first guess at the potential is generally available from the potential of the last model created, so on a good laptop a new model can be computed in only ~ 5 minutes. After computing the self-consistent potential, AGAMA computes one-dimensional velocity distributions at 35 locations (R, z) that are the barycentres of spatial bins into which the Gaia stars have been grouped. In Figs. 10 – 12 these locations (R, z) are shown at the bottom of the V_z panels – Table 2 gives the bin boundaries. The black histograms in Figs. 10 – 12 show the velocity distribution of RVS sample stars. We show histograms for only 12 of the 35 bins, being alternate bins in both R and $|z|$. The top left corner of each panel shows the mean and standard deviation of the histogram. The small, varying non-zero means of V_R and V_z must arise from a combination of the Galactic bar and non-equilibrium dynamics. The red curves in Figs. 10 – 12 show the velocity distributions computed by AGAMA, normalised to the same number of stars as the corresponding black histogram.

Experiments with automatic optimisation of the parameters by the Nelder-Mead downhill simplex algorithm (e.g. Press et al. 1986) were unsuccessful in that the machine proved unable to find a convincing DF in an acceptable number of iterations. It seems that the high dimension of the relevant parameter space combined with the cost of each model evaluation (which arises more from computation of diagnostics than from model construction) sets a requirement for a more sophisticated machine-learning algorithm than naive least-squares minimisation. Therefore we now present a model that has been fitted by hand to the Gaia data and the vertical stellar density profile of Gilmore & Reid (1983). Table 3 lists the values of the parameters that define the model. Fig. 13 shows the density of the stars and dark halo in the meridional plane.

The lower block of panels in Fig. 11 breaks the model velocity histograms for the solar cylinder into the contributions of each stellar component. The full blue curve of the young disc only dominates at the core of the V_z distribution, while the thick disc dominates in the wings and furthest from the plane everywhere except in the V_ϕ histogram, where at small V_ϕ the stellar halo dominates. The values of J_{z0} listed in Table 3 show a six-fold increase in J_{z0} between the thick disc and the old disc, whereas the characteristic actions J_{r0} that control the in-plane dispersions increase by a factor of six only between the young disc and the thick disc. Another noteworthy trend among the parameters are the steady increases in the values of p_r and p_z as one passes from the young disc to the thick disc. That is, the decrease outwards of the velocity dispersions is steeper in older components.

When fitting models by hand, velocity histograms like those shown in Figs. 10 to 12 yield numerous clues for pa-

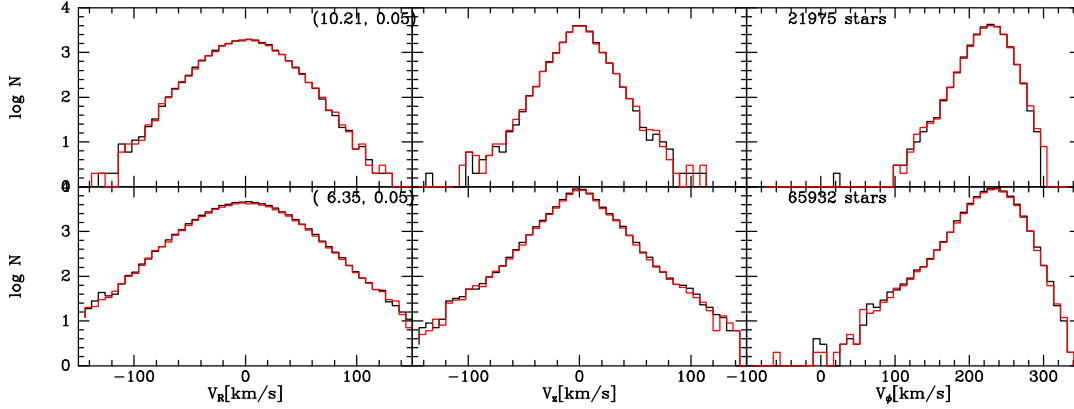


Figure 9. The impact of observational uncertainty on velocity histograms. The black histograms show the result of plotting a sample drawn from a realistic model without allowing for errors, while the red histograms are obtained from the same sample after scattering by typical Gaia DR2 errors. Both rows are for bins with $|z| < 0.1$ kpc but the upper row is for a bin at $R - R_0 \sim 2$ kpc, while the lower row is for the bin at $R - R_0 \sim -2$ kpc.

Table 3. DFs fitted to Gaia data. Normalisations in $10^{10} M_\odot$, actions in kpc km s^{-1}

Spheroids	Mass	J_c	J_0	J_{cut}	α	β	δ	F_{in}	F_{out}	L_0
Dark halo	98	100	10000	20000	1.6	2.7	2	1.4	1.2	100000
Stellar halo	0.1	5	600	100000	1	3.5	2	1.8	1.2	100000
Bulge	1.1	5	19.5	200	0.5	1.8	2	3	2	100000

Discs	Mass	$J_{\phi 0}$	J_{r0}	J_{z0}	p_r	p_z	J_{d0}	J_{v0}
Young disc	0.175	650	10	0.65	-0.7	-0.3	10	100
Middle disc	0.75	600	17	2.8	-0.35	-0.1	10	700
Old disc	1.0	550	22	5	-0.25	-0.1	10	700
Thick disc	0.95	400	63	30	0.13	0.05	20	40

parameter improvement. Most fundamentally, the location of the bumps in the V_ϕ histograms at bottom right indicate how good the model’s circular-speed profile is. This informs the choice of the normalisations of the principal components (dark halo, bulge, discs). The widths of the V_R distributions shown in the left columns of Figs. 10 to 12 guide choices of the parameters J_{r0} of the disc DFs, with the youngest disc dominating the histograms for low $|z|$ (bottom left panels) and the thick disc dominating the histograms at top left. Any tendency for the model V_R histograms to be less satisfactory at an inner radius than at an outer one is addressed by adjusting the relevant p_r parameter. Similarly, the V_z histograms guide choices of J_{z0} , and p_z . Well above the plane, the model V_ϕ histograms have a flat section at low V_ϕ and a bump. The lower block of panels in Fig. 11 shows that the flat section is contributed by the stellar halo, while the bump is dominated by the thick disc. The balance between these two features guides choices of the normalisation of the stellar halo.

Further clues to parameter choice can be drawn from Fig. 14, which shows, in blue, the densities contributed at different distances from the plane by the disc components (full curve: young disc; dotted: middle-aged disc; short-dashed: old thin disc; long-dashed: thick disc). The dashed black and dotted red curves, show the contributions of the dark and stellar halos, respectively. The full black curve shows the sum of the stellar components, which may be compared with the data shown by red dots and black squares.

The red points are from Gilmore & Reid (1983), while the black squares show the double-exponential fit of Jurić et al. (2008). Both sets of points can be shifted vertically at will. To make the full black curve pass through the red data points, one has to adjust the normalisations of the dark halo and the discs, and also the disc parameters J_{z0} , in the choice of which Fig. 11 provides additional guidance. Crucially, the middle panels of Figs. 10 to 12 effectively fix the J_{z0} parameters, so the only way to address the model density falling off too steeply with z is to weaken the gravitational field near the plane by shifting mass from the disc to the dark halo. Hence, if the black squares from the SDSS survey were trusted more than the work of Gilmore & Reid (1983), one would make the dark halo more massive and the disc less massive.

Comparison of the red model predictions and the black Gaia histograms in Figs. 10 to 12 shows a considerable measure of agreement between the model and the data at each of the 12 locations shown; plots for the remaining 23 locations considered show a similar level of agreement.

4.4.1 Weaknesses of the fits

In the top-centre panels of Figs. 10 and 11, the red model curves are narrower than the black data curves. The only significant contributors to these curves are the thick disc, which dominates at $|V_z| < 90 \text{ km s}^{-1}$, and the stellar halo. This

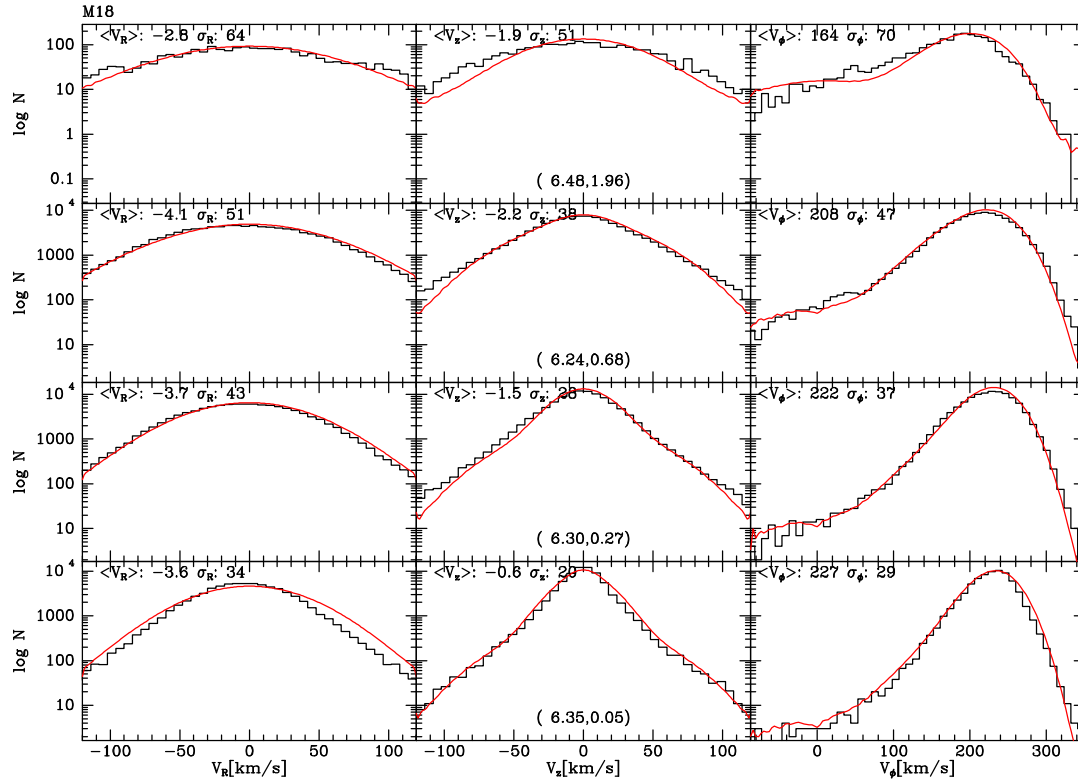


Figure 10. Black histograms show Gaia data for stars with radii $R - R_0 \in (-3, -1.5)$ kpc and distances from the plane that increase from bottom to top (barycentres of the cells are given at upper right of the cells in the first two columns). Means and standard deviations of the velocities are given at top left of each panel. From left to right the columns are for V_R , V_z and V_ϕ . The red curves show the predictions of the dynamical model with the total number of stars in a cell normalised to agree with the data. No allowance has been made for observational errors. M18 at top left in this and subsequent figures is simply the model's designation.

problem might be addressed by reducing the thick disc's value of p_z .

In the bottom left panel of Fig. 10 the red model curve lies above the black data curve. The thick, middle and old discs all make significant contributions to the wings of these curves. The problem could be addressed by lowering J_{r0} for the middle disc at the risk of spoiling agreement in other panels.

In Figs. 10 to 12 the red curves for V_ϕ have a tendency to be too high at $V_\phi < 0$. It would be unwise to take the model's predictions for stars of low V_ϕ too seriously because stars that approach the Galactic centre must be influenced by the Galactic bar, which is not included in the model. However, the model's prediction of a surfeit of stars at $V_\phi < 0$ is least apparent in Fig. 10 for the bins closest to the centre, where the bar should be most influential. The red curves for V_ϕ in the top-right panels of Figs. 10 to 12 are dominated by the stellar halo, which we have modelled as a non-rotating component because many studies (e.g. Schönrich et al. 2014, and references therein) have concluded that this is so. So perhaps one should revisit the issue of halo rotation in light of these Gaia data: the outer halo may be non-rotating (or even counter-rotating (Carollo et al. 2007)) but the inner halo may rotate detectably. In any event, ours is a very basic model of the stellar halo, that cannot address the empirical chemodynamical dichotomy into fairly isotropic, metal-poor and radially biased, metal-rich components (Helmi et al. 2018; Belokurov et al. 2018). Such a model must await res-

Table 4. Densities in the MW model in $M_\odot \text{pc}^{-3}$ or $M_\odot \text{pc}^{-2}$ ($1 \text{ GeV cm}^{-3} = 0.0263 M_\odot \text{pc}^{-3}$).

	gas	stars	DM	Total
$\Sigma(R_0, 1.1 \text{ kpc})$	13.6	21.6	26.0	61.2
$\rho(R_0, 0)$	0.057	0.0317	0.0121	0.0436

olution of the issue regarding choice of DFs discussed by Binney (2022).

4.4.2 Predictions of the models

The full black curve in Fig. 15 shows the circular-speed curve of the gravitational potential that emerges from the choices made for the DF by the self-consistency condition. After optimising agreement between model and data in the earlier figures, the model does not have freedom to adjust this curve, so it is a significant result that it agrees remarkably well with the data points from other recent work, including the Wegg & Gerhard (2013) dynamical model of the bar/bulge, modelling of Cepheid variables by Mróz et al. (2019) and Ablimit et al. (2020) and a study of 23 000 red giants by Eilers et al. (2019). In Fig. 15 the model curve is set by the kinematics of all stars in the restricted radial range $6 \lesssim R \lesssim 12$ kpc rather than by objects presumed to be on near circular orbits over a wider range of radii. The curve extends in to the centre and out to large radii by

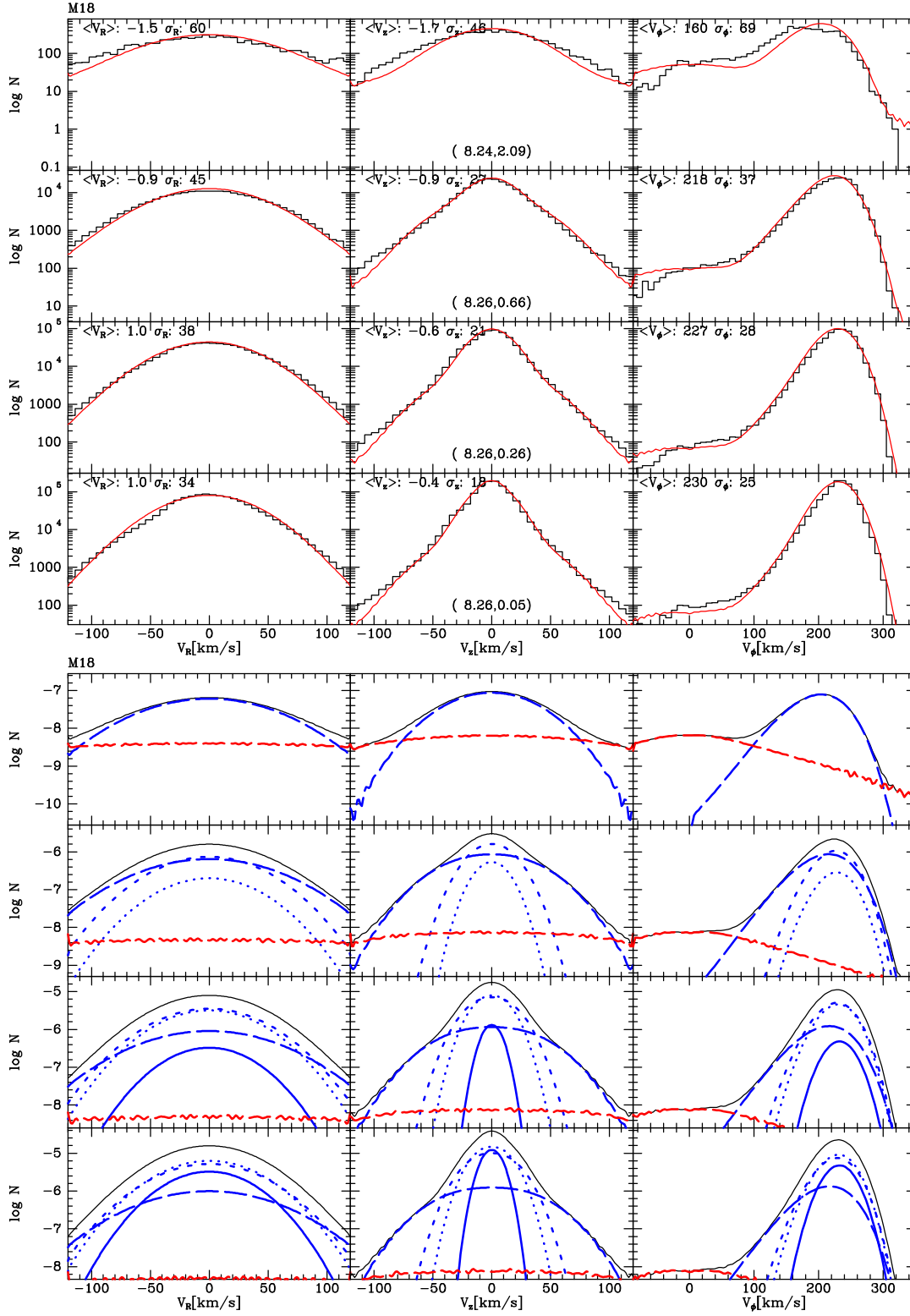


Figure 11. Upper block of panels: the same as Fig. 10 but for $R - R_0 \in (-.5, +0.5)$ kpc. Lower block of panels: how the model histograms above are assembled from the contributions of different components. Blue curves show the disc's contributions (full, dotted and dashed as age increases and long-dashed for the thick disc). The contributions from the bulge and the stellar halo are plotted in heavy black and red, respectively.

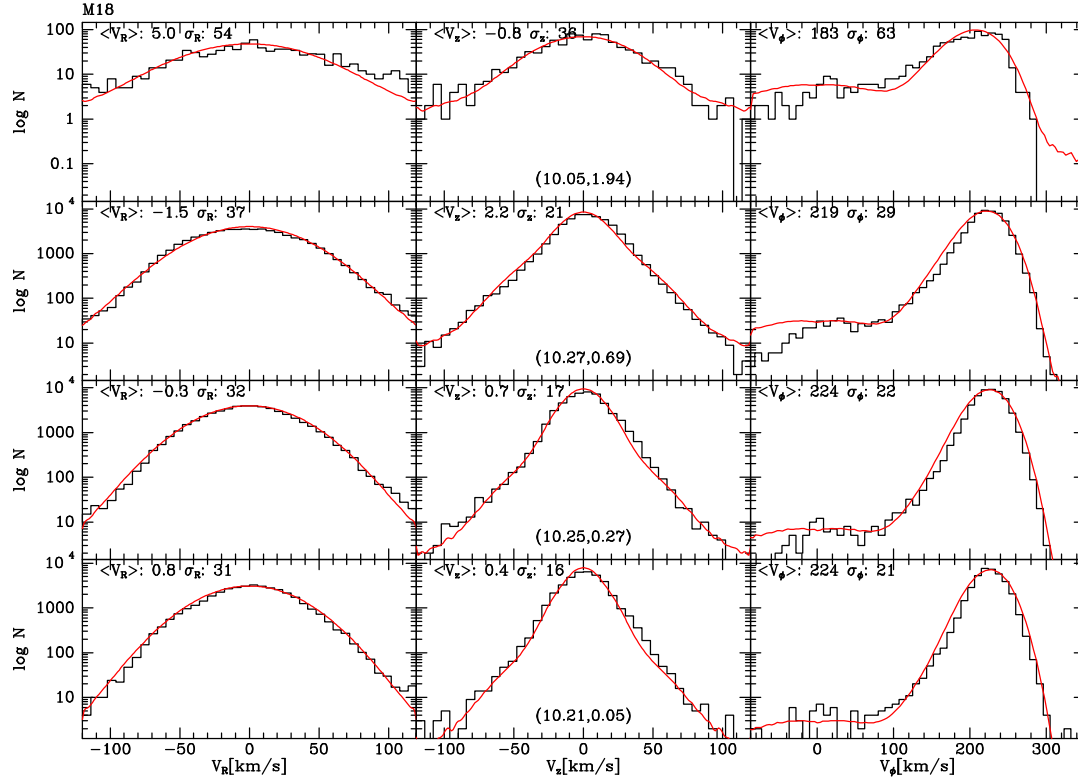


Figure 12. The same as Fig. 10 but for $R - R_0 \in (1.5, 3)$ kpc.

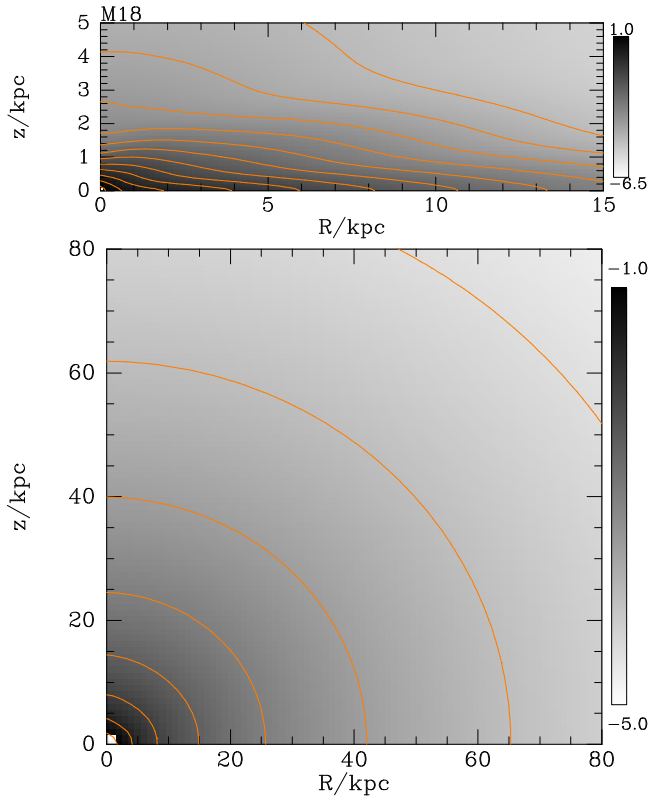


Figure 13. The density in the meridional (R, z) plane of stars (upper panel) and dark matter. The colour scales are logarithmic with two contours per dex.

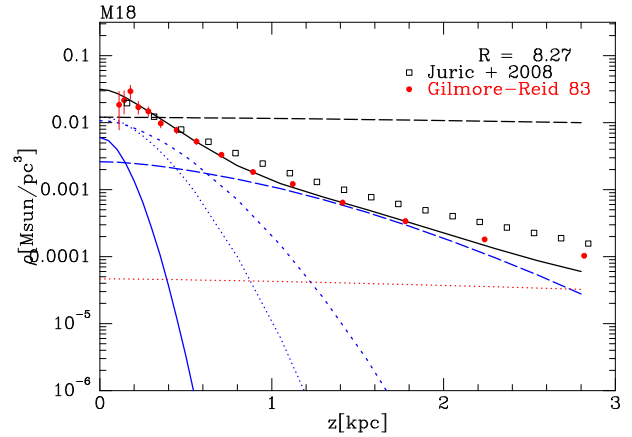


Figure 14. Density as a function of distance from the plane at R_0 . From lower left to upper right, the blue curves show the contributions of the young, middle-aged, old and thick discs. The dotted red curve shows the contribution of the stellar halo and the full black curve shows the sum of stellar contributions. The density of dark matter is shown by the dashed black line. The red data points show the measurements of Gilmore & Reid (1983) while the open squares show the analytic fit to data of Jurić et al. (2008)

virtue of the physical assumptions that underlie the functional forms of the DFs. It runs just above the majority of the data points, but this will to some extent reflect our adoption from Schönrich et al. (2019) of a faster value for the Sun's V_ϕ component than others have used.

In Fig. 15 the dotted blue curve shows the contributions to V_c from stars and gas. Baryons make the largest contribu-

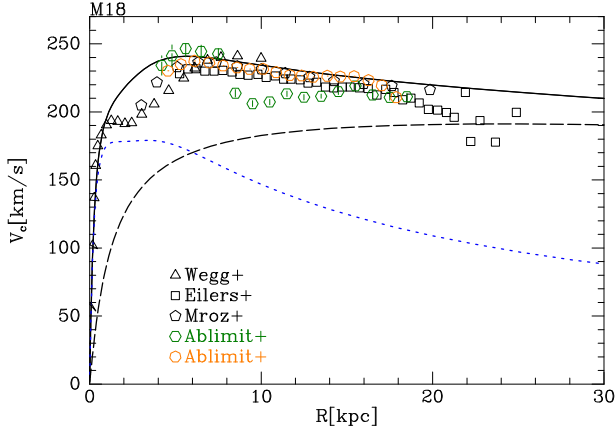


Figure 15. The circular speeds generated by the stars and gas (blue dotted) and dark halo (black dashed) together with the total circular speed (full black). The data points show estimates of V_c from three recent studies. The green circles show values obtained by Ablimit et al. (2020) using only proper motions.

tion to the circular-speed curve within 6 kpc and the bulge contributes more than the disc inside 2.3 kpc. In fact, in the inner kiloparsec the gravitational force from the disc is directed *outwards*, so it actually reduces V_c – see below.

Table 4 gives the local densities of baryons and dark matter according to the model shown here, and also the surface density $\Sigma(R_0, 1.1) = 61.2 \text{ M}_\odot \text{ pc}^{-2}$ of mass that lies within 1.1 kpc of the plane at the solar radius. This comprises $13.6 \text{ M}_\odot \text{ pc}^{-2}$ of gas, $21.6 \text{ M}_\odot \text{ pc}^{-2}$ of stars and $26.0 \text{ M}_\odot \text{ pc}^{-2}$ of dark matter. For comparison, Kuijken & Gilmore (1991), using a sample of K dwarfs, inferred $\Sigma(R_0, 1.1) = 71 \pm 6 \text{ M}_\odot \text{ pc}^{-2}$, while Holmberg & Flynn (2004), using K giants as tracers, obtained $\Sigma(R_0, 1.1) = 74 \pm 6 \text{ M}_\odot \text{ pc}^{-2}$. More recently, by counting stars in Gaia EDR3 Everall et al. (2022a) infer $(23 \pm 2.4) \text{ M}_\odot \text{ pc}^{-2}$ of stars, and by applying the Jeans equations to data from Gaia DR3 Nitschai et al. (2021) find $\Sigma(R_0, 1.1) = (55 \pm 1.7) \text{ M}_\odot \text{ pc}^{-2}$.

Table 4 reports the model’s local density of stars to be $0.0317 \text{ M}_\odot \text{ pc}^{-3}$, which lies below but is consistent with the value $(0.0366 \pm 0.005) \text{ M}_\odot \text{ pc}^{-3}$ Everall et al. (2022a) inferred from Gaia EDR3. The local density of the stellar halo is $4.7 \times 10^{-5} \text{ M}_\odot \text{ pc}^{-3}$. Table 4 reports the local density of dark matter to be $\rho_{\text{DM}}(R_0) = 0.0121 \text{ M}_\odot \text{ pc}^{-3} = 0.46 \text{ GeV cm}^{-3}$. For comparison, from their study of red giants, Eilers et al. (2019) inferred the local density of dark matter to be $0.0079 \pm 0.0008 \text{ M}_\odot \text{ pc}^{-3}$, while Nitschai et al. (2021) obtained $0.0089 \pm 0.0006 \text{ M}_\odot \text{ pc}^{-3}$ and Cautun et al. (2020) found $0.0088 \pm 0.0005 \text{ M}_\odot \text{ pc}^{-3}$. Thus our model is more dark-matter dominated than several recent studies prefer. Evidently we still have some way to go before a consistent picture emerges of the local structure of our Galaxy. A comprehensive review of estimates of the dark halo can be found in de Salas & Widmark (2021).

Given that the circular speed is falling at R_0 , there is scope for confusion in this area because the surface density $\Sigma(z)$ within z of the plane and the vertical acceleration $K_z(z)$ satisfy

$$\Sigma(z) = \frac{1}{2\pi G} \left(K_z + \frac{z}{R} \frac{dV_c^2}{dR} \right). \quad (17)$$

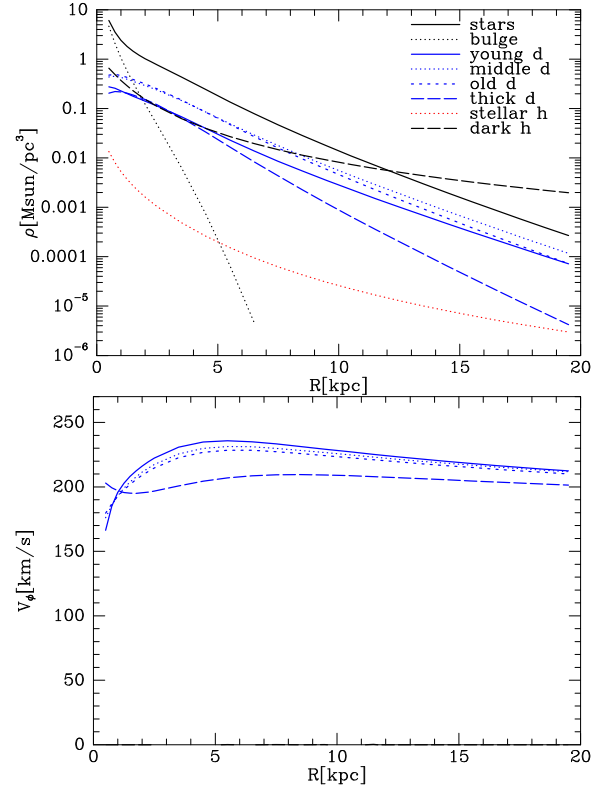


Figure 16. Upper panel: mid-plane densities of each component. Lower panel: mean streaming velocities of disc components. Full black curves are for the young disc, dotted curves are for the middle-aged disc, short-dashed curves are for the old disc and long-dashed curves are for the thick disc. The dotted red curve in the upper panel shows the density of the stellar halo and the full black curve shows the total stellar density. The black long-dashed curves show the densities of the bulge and the dark halo.

Often values of $K_z/(2\pi G)$ are quoted instead of Σ . In the present model $K_z(1.1)/(2\pi G) = 64.1 \text{ M}_\odot \text{ pc}^{-2}$

The full black curve in Fig. 16 shows the sum of the mid-plane densities of all the stellar components. It is very nearly exponential although comprised of contributions that have very different scale-lengths. The steep black, dotted line shows the nearly exponential density of the bulge. At the Sun the dark halo contributes a third of the density contributed by stars.

The lower panel of Fig 16 shows the mean-streaming speeds (V_ϕ) of the stellar discs at the mid-plane. For the thin-disc components $\langle V_\phi \rangle$ is only slightly smaller than V_c , while the value for the thick disc is generally reduced by an asymmetric drift in excess of $> 10 \text{ km s}^{-1}$.

Fig. 17 shows what the Galaxy would look like when seen face-on. The solid blue curve in the left panel shows the contributions of the four disc components while the dotted black curve shows the density obtained on adding the contributions of the bulge and stellar halo. The profiles are not far from exponential.

The dashed red line shows the slope characteristic of a disc with a scale length $R_d = 2.6 \text{ kpc}$, slightly larger than the value $R_d = 2.4 \text{ kpc}$ reported by Robin et al. (2003) from mid-IR photometry. There is a strong correlation between the disc’s scale length and degree of dark-matter domination

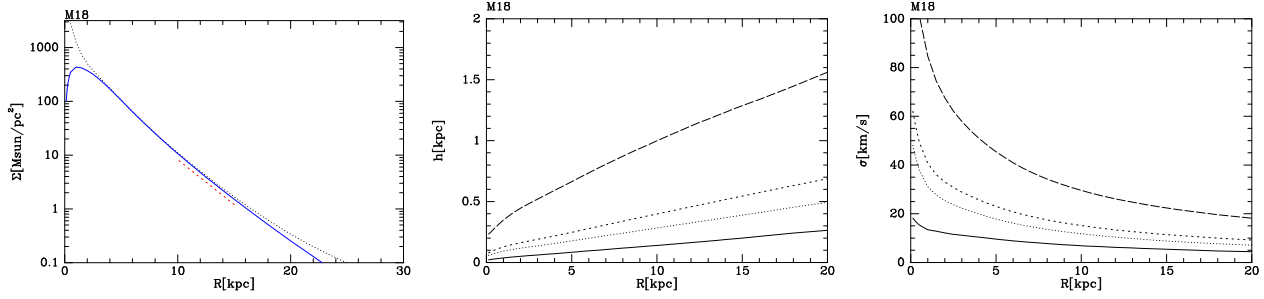


Figure 17. Quantities at face-on projection. Left: the disc’s surface density (solid blue curve) and the surface density including all stellar components (black dotted curve). The dashed red line show the slope of a disc with scale length 2.6 kpc. Centre: rms heights of the disc components (full line for thin disc, dotted for middle disc, short-dashed for old disc and long-dashed for thick disc). Right: projected line-of-sight velocity dispersions of the disc components.

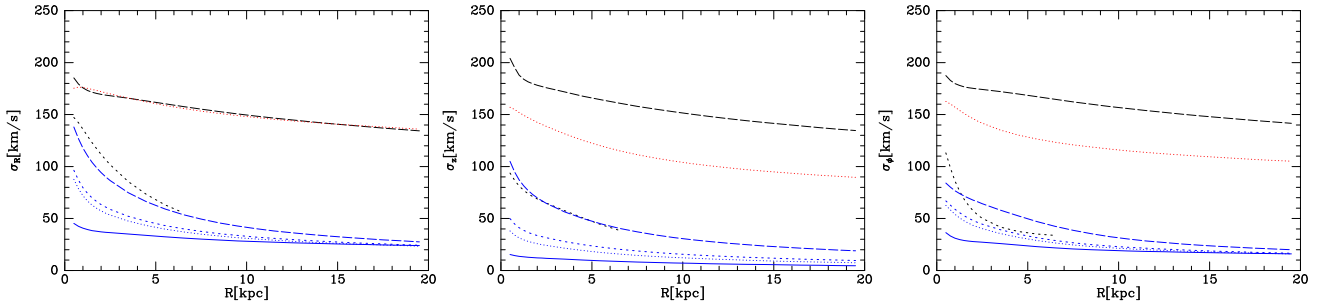


Figure 18. From left to right the radial dependence of the velocity dispersions σ_R , σ_z and σ_ϕ . The black long-dashed curve is for the dark halo, the red dotted curve is for the stellar halo. The dispersions of the discs are given by the four blue curves at the bottom, with the young disc having smallest dispersions and the thick disc the largest. The black dashed curves that reach only to $R = 6$ kpc show the dispersion in the bulge.

in the sense that longer scale lengths imply less dark matter. This correlation is enforced by the radial variation of the circular speed, which is very tightly constrained by the V_ϕ histograms. If one assumes that the dark halo is not too dissimilar to the NFW model (see Section 4.5), then the gentle decline in V_c at $R \gtrsim R_0$ evident in Fig. 15 places an upper limit on the dark halo’s contribution that becomes tighter as R_d grows, and, as explained at the end of Section 4.4, a massive disc is incompatible with the data for the vertical density profile shown in Fig. 14. Thus, ultimately the disc’s vertical density profile at R_0 sets R_d .

The middle panel of Fig. 17 shows the rms thicknesses of the four disc components. All four components become thicker as one moves outwards. The right panel shows the projected line-of-sight velocity dispersions of the disc components, which all increase inwards. The steep central increases in the dispersions of the thin-disc components are associated with the central holes in their surface densities: the blue curves in left panel of Fig. 17 show that the surface density of the stellar discs rises in the inner kiloparsec before flattening, and starting to fall in earnest around $R = 4$ kpc. This structure causes the gravitational field of the stellar disc to be directed *outwards* near the centre. The gas disc, which has a central hole, amplifies this effect.

Fig. 18 shows the radial variation within the plane of the velocity dispersions. At small radii the dark halo has a weak tangential bias that is a consequence of its assumed adiabatic compression by the baryons, and the dispersions fall gently from $> 200 \text{ km s}^{-1}$ at $R \sim 1$ kpc to 120 km s^{-1} at

Table 5. Characteristics of the dark halo. Distances in kpc, masses in $10^{10} M_\odot$.

	r_s	r_{200}	M_{200}
Dark halo	20.0	192	80.5

$R = 20$ kpc. The stellar halo (red dotted curves) is radially biased, with σ_R similar to the dispersions of the dark halo.

The black dotted curves in Fig. 18, which show the velocity dispersions of the bulge, show σ_R and σ_z tracking the dispersions of the thick disc, but σ_ϕ falling much more steeply.

In all disc components $\sigma_R > \sigma_\phi > \sigma_z$, everywhere although σ_R invariably falls faster with increasing R than does σ_z .

4.5 The halo without baryons

Our understanding of the statistical properties of dark haloes depend to a large extent on cosmological simulations that exclude baryons. Comparison of the Galaxy’s dark halo with expectations raised by such simulations requires knowledge of the structure of the dark halo before the baryons fell in. The classic assumption is that the accumulation of baryons was an adiabatic process (Blumenthal et al. 1986; Sellwood & McGaugh 2005). In this case, the primordial structure of the dark halo can be recovered by constructing the self-consistent model defined by the dark halo’s DF

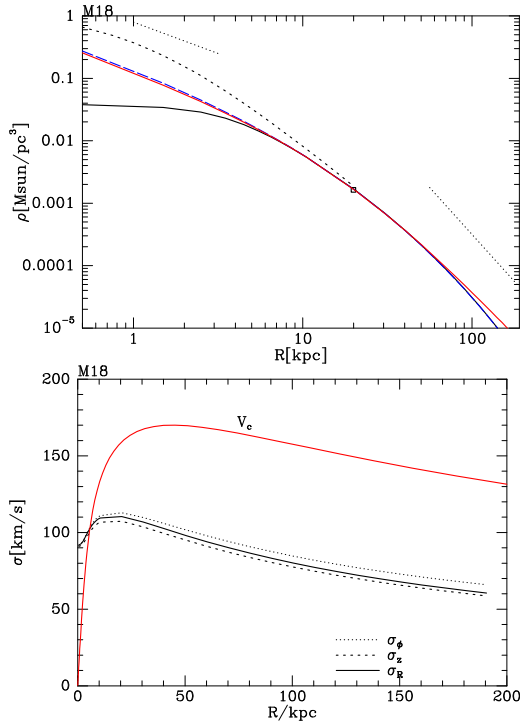


Figure 19. The structure of the dark halo before the infall of baryons. Upper panel: the full black curve shows the density profile generated in isolation by the DF of the Milky Way’s dark halo. The dashed blue curve shows the profile generated by this DF after removal of the Cole–Binney core. The square marks the radius, $r_s = 20.0$ kpc, at which $d \ln \rho / d \ln r = -2$ and the red curve shows the density profile of the NFW halo with the same scale radius. The black dashed curve shows the density of the dark halo as it actually is in the Galaxy. The sloping dotted lines show the asymptotic slopes, -1 and -3 of an NFW profile. Lower panel: the circular speed and the principal velocity dispersions of the halo before removal of the Cole–Binney core.

alone. The full black curve in Fig. 19 shows the structure of this object.

There is now significant evidence that baryonic infall was significantly non-adiabatic (Chan et al. 2015; Pontzen & Governato 2014; Pascale et al. 2018). Indeed it is natural that in the region in which baryons dominate the gravitational field, fluctuations in the gravitational field will have upscattered dark-matter particles, with the consequence that their phase-space density is now lower than it was before the baryons fell in. The Cole–Binney core of our halo is designed to model the consequences of this physics, so to obtain the best estimate of what the dark halo looked like before the baryons fell in, we should remove this core from the DF. The dashed blue curve in Fig. 19 shows the density profile of this primordial dark halo. It closely hugs the red curve, which plots the density of the NFW model that has the same scale radius $r_s = 20$ kpc (the radius at which $d \ln \rho / d \ln r = -2$). This closeness of fit is no accident: the search for a dark halo DF was confined to ones that in isolation generate an NFW profile after removal of the Cole–Binney core. This curve yields $r_{200} = 192$ kpc for the radius at which the mean density is 200 times the mean cosmic density and $M_{200} = 0.805 \times 10^{12} M_\odot$ for the mass interior to that radius. For comparison, Eil-

ers et al. (2019) derive $M_{200} = (0.725 \pm 0.026) \times 10^{12} M_\odot$, while two estimates obtained by Ablimit et al. (2020) are $[r_s = (14.5 \pm 0.5) \text{ kpc}, M_{200} = (0.66 \pm 0.07) \times 10^{12} M_\odot, r_{200} = (179 \pm 5) \text{ kpc}]$ and $[r_s = (14.7 \pm 0.4) \text{ kpc}, M_{200} = (0.82 \pm 0.05) \times 10^{12} M_\odot, r_{200} = (192 \pm 4) \text{ kpc}]$. When comparing these estimates one must bear in mind that the RVS data can constrain the density only at $R \lesssim 12$ kpc, so quoted values of even r_s involve significant extrapolation and values of r_{200} and M_{200} are dangerously exposed to assumptions about the halo’s density profile – for example, the mass of our halo could be made larger either by increasing its truncation action J_{cut} or making its outer slope shallower. The globular cluster system provides some sensitivity to mass that lies beyond $r = 12$ kpc, and from a study of this system Wang et al. (2021) inferred $0.54 \lesssim M_{200}/10^{12} M_\odot \lesssim 0.78$. Using both globular clusters and dwarf spheroidal galaxies, and taking into account perturbation by the LMC, Correa Magnus & Vasiliev (2022) finds $M_{200} = (0.7\text{--}1.6) \times 10^{12} M_\odot$. Whereas our estimates are based on a reconstruction of the dark halo prior to baryon infall, those of earlier work relate to models of the halo as it now is.

The dashed curve in the upper panel of Fig. 19 shows the dark halo’s current density profile; despite the upscattering of dark-matter particles, the gravitational pull of the baryons has more than tripled its density at $R \simeq 1$ kpc from what it was even before the upscattering. The density enhancement remains significant out to r_s . Comparing the current of the dashed and full black curves in the upper panel of Fig. 19 we see that the widespread assumption that the dark haloes of luminous galaxies have NFW profiles is indefensible. Dark haloes will have such profiles only if upscattering of dark-matter particles precisely cancels adiabatic compression, and there are no grounds for believing this to be true. For more on this topic, see Cautun et al. (2020).

The lower panel of Fig. 19 plots velocities associated with this reconstruction of the primordial dark halo. Its circular speed, plotted in red, peaks at 170 km s^{-1} and its velocity distribution is nearly isotropic. Removal of the core changes the dispersions negligibly at $R \gtrsim 5$ kpc.

4.6 Chemodynamics

Fig. 4 of Hayden et al. (2015) is one of the most significant products of the APOGEE survey (Majewski et al. 2017). It shows the distribution of stars in the $([\alpha/\text{Fe}], [\text{Fe}/\text{H}])$ plane in each of 18 bins in the (R, z) plane. The robustness of this result was recently confirmed by Eilers et al. (2022). The upper block of panels in Fig. 20 is an analogous plot using the same data, kindly supplied by M. Hayden. Two stellar populations are clearly visible. There is a high- α population that always occupies the same location in the chemical plane but is much more prominent at large $|z|$ and small R : it has essentially disappeared at $R > 10$ kpc and is very faint at $|z| < 3$ kpc. The other, normal- α , population dominates near the plane and at large R . It moves to lower $[\text{Fe}/\text{H}]$ with increasing R .

If we conjecture how the stellar populations of our dynamical model are distributed in the chemical plane, we can create a analogous figure. The lower block of panels in Fig. 20 shows the result of doing this as follows.

At the centre of each spatial bin we determined the fractional contribution to the stellar density by stars be-

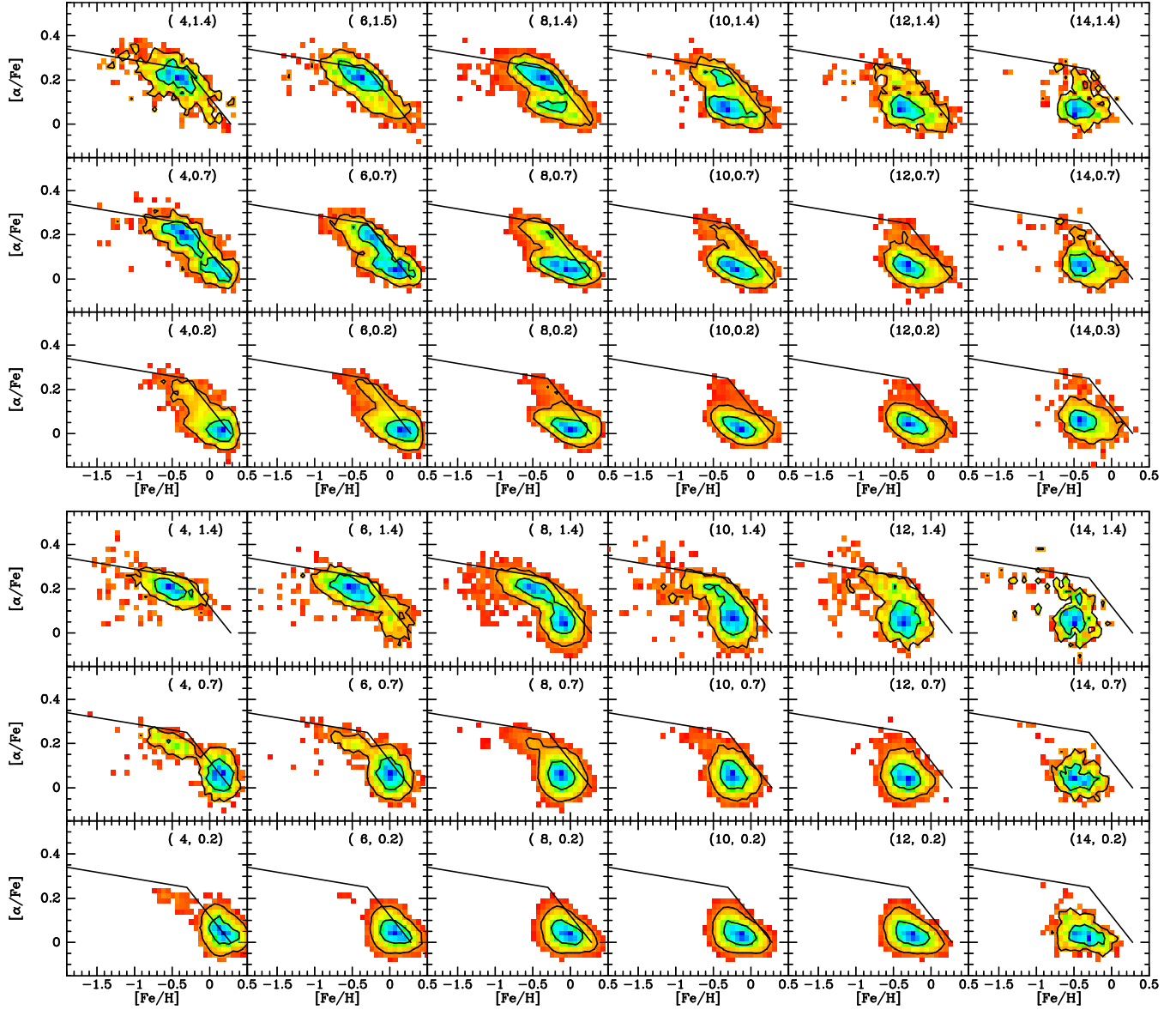


Figure 20. Upper block of panels: a plot analogous to Fig. 4 in Hayden et al. (2015) using the same APOGEE data. Lower block: a similar plot computed from our dynamical model using the chemical compositions of the components given by equations (18) to (21). The mean values of R and z for the stars/pseudo-stars that fall in each spatial bin are given at upper right of each panel. Contours are drawn that enclose 90 percent and 50 percent of stars.

longing to each of the six populations, young disc, middle disc, old disc, thick disc, stellar halo and bulge. Then mock stars were drawn from the velocity distributions of the components in the corresponding proportions, the total number of stars being the same as the number of real stars reported by Hayden et al. (2015) for that spatial bin. The mock stars were assigned values of $[\text{Fe}/\text{H}]$ and $[\alpha/\text{Fe}]$ by sampling its component's chemical pdf. Each pdf was a two-dimensional Gaussian with principal axes

$$\begin{pmatrix} x \\ y \end{pmatrix} = \begin{pmatrix} \cos \theta & -\sin \theta \\ \sin \theta & \cos \theta \end{pmatrix} \begin{pmatrix} [\text{Fe}/\text{H}] \\ [\alpha/\text{Fe}] \end{pmatrix} \quad (18)$$

that are rotated with respect to the $[\text{Fe}/\text{H}]$ and $[\alpha/\text{Fe}]$ axes. The angle θ being small, x is close to $[\text{Fe}/\text{H}]$ while y is close to $[\alpha/\text{Fe}]$.

In the normal- α components, the distribution in y was independent of J_ϕ but the mean value of x was taken to be

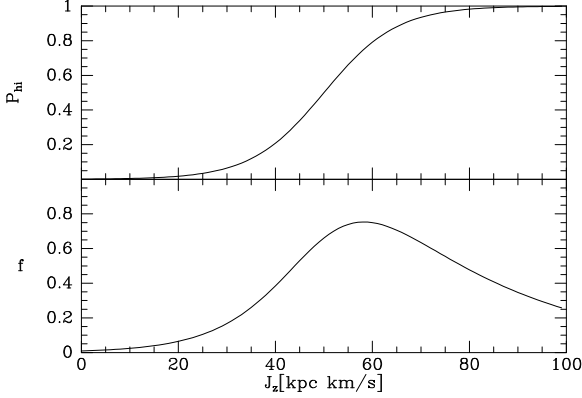
$$\bar{x} = \bar{x}_\odot + \frac{d\bar{x}}{dJ_\phi} (J_\phi - J_{\phi\odot}), \quad (19)$$

where $J_{\phi\odot}$ is the circular angular momentum at the Sun and \bar{x}_\odot is approximately the mean metallicity of the component at R_0 . This dependence of \bar{x} on J_ϕ generates a metallicity gradient $d[\text{Fe}/\text{H}]/dR \simeq V_c d\bar{x}/dJ_\phi$ in the disc.

The top row of Fig. 20 shows that the high- α population is scarcely visible at $R \gtrsim 10$ kpc. The obvious way to engineer this fading of the high- α is to make the probabil-

Table 6. Parameters of the chemical pdfs used to construct Fig. 20. The units of x, y, σ_x, σ_y are dex, those of $V_c d\bar{x}/dJ_\phi$ are dex per kpc, those of θ are degrees and those of J_{z0} and Δ_z are kpc km s^{-1} .

Component	\bar{x}_\odot	$V_c d\bar{x}/dJ_\phi$	\bar{y}	σ_x	σ_y	θ	J_{z0}	Δ_z
Young disc	0.2	-0.07	0	0.1	0.03	2	-	-
Middle disc	0	-0.07	0.03	0.1	0.03	2	-	-
Old disc	-0.2	-0.07	0.06	0.1	0.05	2	-	-
Thick disc	-0.5	0	0.2	0.2	0.03	7	50	15
Stellar halo	-1	0	0.2	0.3	0.1	3	-	-
Bulge	-0.5	0	0.2	0.2	0.02	3	-	-

**Figure 21.** Upper panel: the probability that a thick-disc star has high- α chemistry. Lower panel: the J_z -dependence of the DF of the high- α population.

ity P_{hi} of a thick-disc star belonging to this population a function of J_ϕ . However experiments with P_{hi} of the form

$$P_{\text{hi}} = \frac{1}{2} \left[1 - \tanh \left(\frac{J_\phi - J_{\phi 0}}{\Delta_\phi} \right) \right], \quad (20)$$

produced results that were unsatisfactory in two respects: i) an implausibly rapid transition was required, specifically $J_{\phi 0}/\Delta_\phi \geq 100$, and ii) it left the high- α population too prominent at $z \simeq 0.7$ and 0.2 kpc. The more satisfactory results shown in the lower block of panels of Fig. 20 were obtained by taking the probability of belonging to the high- α population to be

$$P_{\text{hi}}(J_\phi) = \frac{1}{2} \left[1 + \tanh \left(\frac{J_z - J_{z0}}{\Delta_z} \right) \right]. \quad (21)$$

Now $P_{\text{hi}} \simeq 1$ for $J_z \gg J_{z0}$ and $P_{\text{hi}} \simeq 0$ for $J_z \ll J_{z0}$. If a star was assigned to the high- α portion of the thick disc, its chemistry was drawn from a Gaussian in (x, y) independently of J_ϕ , while if it was assigned to the normal- α disc, its chemistry was determined as if it were a member of the old disc. The upper panel of Fig. 21 is a plot of $P_{\text{hi}}(J_z)$ for the chosen values of J_{z0} and Δ_z .

Table 6 lists for each component the numbers that define the two-dimensional Gaussian pdfs, and the parameters J_{z0} and Δ_z that determine the distribution of high- α stars within the thick disc. Comparison of the upper and lower blocks of panels in Fig. 20 shows that the model captures the essential features of the observations, including the dominance of the high- α population at small R and large z , and the drift of the normal- α population towards lower $[\text{Fe}/\text{H}]$ with increasing R .

5 DISCUSSION

5.1 Extracting information from data

Much previous galaxy modelling has been based on the Jeans equations (Binney et al. 1990; Robin et al. 2003; Garbari et al. 2012; Read & Steger 2017; Nitschai et al. 2020, 2021; Sivertsson et al. 2022). Gaia produces such large samples that the full distribution of velocities in a small spatial region can be determined with exquisite precision. These distributions are highly non-Gaussian, so a technique which characterises them by just two or three moments is throwing away valuable information.

Extraction of the maximum information from a stellar survey is probably achieved by evaluating the likelihood of the survey data given candidate models. Unfortunately, this technique is unfeasible when there is significant obscuration by dust and the density of dust is not well known (e.g. Li & Binney 2022b). Moreover, evaluating likelihoods for individual stars is very costly for samples as large as those yielded by Gaia. In light of these considerations there is a compelling case for binning stars spatially and evaluating the fit to models of the resulting velocity distributions. The comparison would be better made by evaluating likelihoods in velocity space than by binning stars by their single velocity components, but the cost of likelihood evaluation seems currently prohibitive. Humans can more easily assess fit quality from one-dimensional velocity distributions than from three-dimensional ones, but for an MCMC search of model space one should probably bin stars into cell in velocity space that are not the two-dimensional slices right across the space employed here.

5.2 The dark-matter baryon balance

Hand-fitting models to the data reveals a strong connection between the radial structure of the dark halo and the extent to which the disc is self-gravitating. On the one hand, the large distances from the plane reached by thick-disc stars places an upper limit on the disc's mass. On the other hand, the clear outwards decline in the circular speed at $R \gtrsim 6$ kpc requires both a significant contribution to the gravitational field from stars, and that the circular speed contributed by the dark halo does not rise strongly in this radial range. The latter requirement places an upper limit on the core parameter J_c , and a lower limit on the index α of the dark halo's DF. It would be very interesting to use the MCMC algorithm to explore how big a region of model space acceptable models occupy.

5.3 We need better halo DFs

Action-based DFs that envisage a non-zero density of stars in the neighbourhood of $J_\phi = 0$ need to conform to certain constraints (Piffl et al. 2015; Binney 2022). The disc DFs introduced here have vanishing star densities at $J_\phi = 0$ so do not need to engage with these constraints, but the spheroidal DFs of the dark halo, the bulge and the stellar halo should conform to these constraints, and they do so to only a limited extent. To avoid excessive violation of the constraints, and the introduction of unphysical features, the parameters of the spheroidal DFs have been chosen to avoid plausible levels of radial bias. The absence of radial bias in the dark halo and the bulge is not significant observationally because the data contain few bulge stars and no dark-matter particles. But the stellar halo needs to have greater radial bias and work to enable this should be a high priority. Moreover, restricting the velocity anisotropy of the dark halo's DF limits the dark halo's flattening, and a flattened halo will imply a less massive disc. Hence, better functional forms for spheroidal DFs may significantly change our understanding of the disc-halo balance.

5.4 Structure of the high- α population

The quality of the fit to the Hayden et al. (2015) data that is provided by the restriction of high- α stars to orbits with large J_z is so good that it seems certain that the restriction is real, but its historical origin is far from evident. The *a priori* expectation is that high- α stars would be restricted to low $|J_\phi|$ because these would be the first stars to form in the natural inside-out formation picture. However, fruitless attempts to model the data in this way left us convinced that it is to orbits with large J_z that high- α stars are confined.

In light of this result the high- α population would form a very strange component if considered in isolation, for it comprises stars that have apocentres in z that fall in quite a narrow range – the lower panel of Fig. 21 illustrates this fact by showing how the DF of this population depends on J_z . It seems that at low $|z|$ the density of high- α stars *increases* with z , peaking where a star with $J_z \simeq 50 \text{ kpc km s}^{-1}$ turns around.

Could the J_z -distribution of the high- α stars have arisen when a primordial, high- α , thin disc was shattered in a merger (Belokurov et al. 2020)? The problem with this idea is that we would expect the merger to spread stars in J_z rather than shift them all up in J_z , leaving orbits around $J_z = 0$ vacant until occupied by the subsequent formation of low- α stars. A possibly more promising scenario that the high- α stars were stripped from a satellite that was finally disrupted on a nearly circular orbit, and their characteristic value of $J_z \sim 50 \text{ kpc km s}^{-1}$ was the vertical action of the satellite when it dispersed. Another possibility is that we are seeing the result of ‘levitation’ (Sridhar & Touma 1996): stars trapped in a resonance such as $\Omega_r = \Omega_z$ moving up in J_z along with the resonance as the disc gains mass and the values of Ω_z/Ω_r in the plane increase.

5.5 What to do with all Gaia stars

Gaia is a survey instrument that provides photometry of unprecedented precision. Hence it is the ultimate tool with

which to determine how the density of stars varies with location. Yet we have completely neglected this possibility and instead used a forty-year-old determination of the density of stars above the Sun (Gilmore & Reid 1983). The problem is that the Gaia catalogues have complex selection functions. Even after these selection functions have been determined (Everall & Boubert 2022), to predict how many stars will be catalogued at a given sky position one needs accurate knowledge of the extinction as a function of distance along the relevant line of sight. This knowledge is currently woefully lacking for most sight lines, but fortunately along lines of sight at $|b| \gtrsim 80^\circ$ extinction is sufficiently low that a poor understanding of its distribution is not a major problem, so it is possible to deduce the vertical profile $\rho_*(z)$ of the disc near the Sun from Gaia data, and Everall et al. (2022b,a) have recently done this. Their work appeared after the present work was largely completed and a decision was made not to replace the Gilmore & Reid (1983) data with the new determination of $\rho_*(z)$ because it would be fundamentally sounder to fit the self-consistent models directly to Gaia's star counts rather than to a density profile that has been fitted to the star counts – Everall et al. (2022b,a) needed to assume that the luminosity function is independent of z , though it will not be because younger populations are more prominent at low $|z|$, and older and more metal-poor populations dominate at high $|z|$.

Since each population of the current models comes with an age range and therefore a luminosity function, predicting the star counts along a dust-free line of sight is straightforward. Comparison of these star counts, modified by the relevant Gaia selection function, with the actual star counts will then yield a constraint on the models that can replace that provided here by Fig. 14.

Probably the best way to use comparisons between predicted and actual Gaia star counts along general lines of sight is for the construction of a global three-dimensional dust map. Current attempts to construct dust maps are restricted to the tiny fraction of stars for which it is possible to obtain an extinction (Sale & Magorrian 2014; Green 2018; Green et al. 2019; Lallement et al. 2022). Such stars, mainly intrinsically blue stars, are for some reason susceptible to having their absolute magnitudes predicted. A model of the type presented here, combined with a trial dust model, yields for each field of view star counts as a function of parallax that can be compared with the actual star counts down to the faintest magnitudes. Hence every star in the Gaia catalogue can be used to constrain the dust model.

6 CONCLUSIONS

Fully self-consistent dynamical galaxy models constitute valuable tools for the interpretation of observational data for both our Galaxy and external galaxies because they pull constraints from a variety of observational probes into a coherent physical framework. They minimise the number of parameters that must be determined from observations by exploiting to the full the constraints imposed by the laws of dynamics.

Such models are inherently steady-state models, and currently AGAMA can only construct axisymmetric models. However, from such a model one may easily draw an N-body

sample, and by perturbing this either study time-dependent phenomena (e.g. Binney & Schönrich 2018; Al Kazwini et al. 2022) or construct barred models by the made-to-measure technique (Syer & Tremaine 1996; de Lorenzi et al. 2007).

Hitherto, self-consistent models of our Galaxy (Piffl et al. 2015; Binney & Piffl 2015; Cole & Binney 2017) have represented the discs with the quasi-exponential DF. Unfortunately, the radial and vertical epicycle frequencies $\kappa(J_\phi)$ and $\nu(J_\phi)$, and the circular radius $R_c(J_\phi)$ play significant roles in this DF, so the DF is only fully specified when a potential is given. This fact makes the quasi-isothermal DF ill-suited to self-consistent galaxy modelling because the galaxy’s potential should emerge from the DF, not precede it.

Therefore in Section 2 we introduced a new family of DFs for discs that are fully specified by the disc’s mass and the values of seven parameters. We have elucidated the physical significance of the parameters: three characteristic actions set the scale length of the disc and the in-plane and vertical velocity dispersions. Two further parameters set the radial gradients of the dispersions and the final two control the central structure of the disc.

In Section 4 we built a model of our Galaxy that comprises four of these stellar discs, a gas disc, and three spheroidal components. The model reproduces to good accuracy the velocity distributions of stars in the Gaia RVS sample at 35 locations distributed through the rectangle $R_0 \pm 3$ kpc and $|z| \leq 3$ kpc. It also fits old observations of the density of stars as a function of $|z|$ in the column above the Sun, which effectively set the balance between baryon and dark mass.

The model’s circular-speed curve is tightly constrained over the ~ 6 kpc radial range covered by the Gaia RVS sample and it agrees well with recent determinations using specific tracer populations. Its stellar disc has mass $3.9 \times 10^{10} M_\odot$, scale length 2.6 kpc and local surface density $22 M_\odot \text{pc}^{-2}$. Its dark halo has mass $M_{200} = 80.5 \times 10^{10} M_\odot$, scale radius $r_s = 20$ kpc and local density $0.012 M_\odot \text{pc}^{-3}$. Its original central cusp is assumed to have been eroded by interactions with baryons. We reconstructed the dark halo prior to baryon infall. Prior to the addition of baryons it had peak circular speed 170 km s^{-1} and virial radius $r_{200} = 192$ kpc.

The model’s stellar disc is a superposition of three relatively cool “thin” discs of increasing velocity dispersions and therefore thickness, and a much hotter and thicker disc. The disc’s scale lengths decrease as their dispersions and thicknesses increase. The hotter a disc is, the faster its velocity dispersions fall off with increasing radius.

After assigning a chemical composition to each of the model’s six stellar components, we could predict from the model how the chemistry of stars varies with location in the Rz plane. We identified simple compositions of the components that yielded good agreement between the model’s predictions and the chemistry measured by the APOGEE survey (Hayden et al. 2015). The key feature of these compositions is the restriction of high- α stars to orbits with high J_z . This restriction ensures that normal- α stars dominate both at low $|z|$ and small R , and at high $|z|$ and large R .

The Galaxy model presented here is designed mainly to illustrate the opportunities that are opened up by the new disc DFs. There is much scope to extend the work by a

wider exploration of model space and the addition of more and better observational constraints.

Here we have presented a single model that provides good fits to most of the data. Attempts to find a best-fitting model were unsuccessful on account of the high dimensionality of the model parameter space and the cost of computing observables from a model. Nevertheless, soon the MCMC algorithm should be used to explore model space starting from this model and thus to obtain insight into the range of model parameters that generate acceptable models.

ACKNOWLEDGEMENTS

This work was supported by the UK Science and Technology Facilities Council under grant number ST/N000919/1. JB also acknowledges support from the Leverhulme Trust through an Emeritus Fellowship. We thank Michael Hayden for providing the APOGEE data re-plotted in Fig. 20.

This work presents results from the European Space Agency (ESA) space mission Gaia. Gaia data are being processed by the Gaia Data Processing and Analysis Consortium (DPAC). Funding for the DPAC is provided by national institutions, in particular the institutions participating in the Gaia MultiLateral Agreement (MLA). The Gaia mission website is <https://www.cosmos.esa.int/gaia>. The Gaia archive website is <https://archives.esac.esa.int/gaia>.

DATA AVAILABILITY

The code that generates Galaxy models can be downloaded from the AGAMA website <https://github.com/GalacticDynamics-Oxford/Agama>

REFERENCES

- Abazajian K. et al., 2003, *AJ*, 126, 2081
- Ablimit I., Zhao G., Flynn C., Bird S. A., 2020, *ApJL*, 895, L12
- Al Kazwini H. et al., 2022, *A&A*, 658, A50
- Antoja T. et al., 2018, *Nat*, 561, 360
- Belokurov V., Erkal D., Evans N. W., Koposov S. E., Deason A. J., 2018, *MNRAS*, 478, 611
- Belokurov V., Sanders J. L., Fattahi A., Smith M. C., Deason A. J., Evans N. W., Grand R. J. J., 2020, *MNRAS*, 494, 3880
- Binney J., 2010, *MNRAS*, 401, 2318
- Binney J., 2012, *MNRAS*, 426, 1328
- Binney J., 2014, *MNRAS*, 440, 787
- Binney J., 2022, in preparation, xxx
- Binney J., McMillan P., 2011, *MNRAS*, 413, 1889
- Binney J., Piffl T., 2015, *MNRAS*, 454, 3653
- Binney J., Schönrich R., 2018, *MNRAS*, 481, 1501
- Binney J. J., Davies R. L., Illingworth G. D., 1990, *ApJ*, 361, 78
- Blumenthal G. R., Faber S. M., Flores R., Primack J. R., 1986, *ApJ*, 301, 27
- Boubert D., Everall A., 2020, *MNRAS*, 497, 4246
- Bovy J., Rix H.-W., 2013, *ApJ*, 779, 115
- Carollo D. et al., 2007, *Nat*, 450, 1020
- Cautun M. et al., 2020, *MNRAS*, 494, 4291

- Chan T. K., Kereš D., Oñorbe J., Hopkins P. F., Muratov A. L., Faucher-Giguère C. A., Quataert E., 2015, *MNRAS*, 454, 2981
- Cole D. R., Binney J., 2017, *MNRAS*, 465, 798
- Correa Magnus L., Vasiliev E., 2022, *MNRAS*, 511, 2610
- de Lorenzi F., Debattista V. P., Gerhard O., Sambhus N., 2007, *MNRAS*, 376, 71
- de Salas P. F., Widmark A., 2021, *Reports on Progress in Physics*, 84, 104901
- Dehnen W., Binney J., 1998, *MNRAS*, 294, 429
- Eilers A.-C., Hogg D. W., Rix H.-W., Ness M. K., 2019, *ApJ*, 871, 120
- Eilers A.-C., Hogg D. W., Rix H.-W., Ness M. K., Price-Whelan A. M., Mészáros S., Nitschelm C., 2022, *ApJ*, 928, 23
- Everall A., Belokurov V., Evans N. W., Boubert D., Grand R. J. J., 2022a, *MNRAS*, 511, 3863
- Everall A., Boubert D., 2022, *MNRAS*, 509, 6205
- Everall A., Boubert D., Koposov S. E., Smith L., Holl B., 2021, *MNRAS*, 502, 1908
- Everall A., Evans N. W., Belokurov V., Boubert D., Grand R. J. J., 2022b, *MNRAS*, 511, 2390
- Gaia Collaboration et al., 2021, *A&A*, 649, A8
- Gaia Collaboration, Brown A. G. A. e. a., 2018, *A&A*, 616, A1
- Gaia Collaboration, Katz D. e. a., 2018, *A&A*, 616, A11
- Garbari S., Liu C., Read J. I., Lake G., 2012, *MNRAS*, 425, 1445
- Gilmore G., Reid N., 1983, *MNRAS*, 202, 1025
- Green G. M., 2018, *Journal of Open Source Software*, 3, 695
- Green G. M., Schlafly E., Zucker C., Speagle J. S., Finkbeiner D., 2019, *ApJ*, 887, 93
- Hayden M. R. et al., 2015, *ApJ*, 808, 132
- Helmi A., Babusiaux C., Koppelman H. H., Massari D., Veljanoski J., Brown A. G. A., 2018, *Nat*, 563, 85
- Holmberg J., Flynn C., 2004, *MNRAS*, 352, 440
- Hunt J. A. S., Bub M. W., Bovy J., Mackereth J. T., Trick W. H., Kawata D., 2019, *MNRAS*, 490, 1026
- Jurić M. et al., 2008, *ApJ*, 673, 864
- Kuijken K., Gilmore G., 1991, *ApJL*, 367, L9
- Lallement R., Vergely J. L., Babusiaux C., Cox N. L. J., 2022, *arXiv e-prints*, arXiv:2203.01627
- Li C., Binney J., 2022a, *MNRAS*, 510, 4706
- Li C., Binney J., 2022b, *arXiv e-prints*, arXiv:2205.01455
- Majewski S. R. et al., 2017, *AJ*, 154, 94
- Malhotra S., 1995, *ApJ*, 448, 138
- Mróz P. et al., 2019, *ApJL*, 870, L10
- Nitschai M. S., Cappellari M., Neumayer N., 2020, *MNRAS*, 494, 6001
- Nitschai M. S., Eilers A.-C., Neumayer N., Cappellari M., Rix H.-W., 2021, *ApJ*, 916, 112
- Pascale R., Posti L., Nipoti C., Binney J., 2018, *MNRAS*, 480, 927
- Piffl T. et al., 2014, *MNRAS*, 445, 3133
- Piffl T., Penoyre Z., Binney J., 2015, *MNRAS*, 451, 639
- Pontzen A., Governato F., 2014, *Nat*, 506, 171
- Posti L., Binney J., Nipoti C., Ciotti L., 2015, *MNRAS*, 447, 3060
- Press W. H., Flannery B. P., Teukolsky S. A., 1986, *Numerical recipes. The art of scientific computing*. Cambridge: University Press, 1986
- Read J. I., Steger P., 2017, *MNRAS*, 471, 4541
- Reid M. J., Brunthaler A., 2004, *ApJ*, 616, 872
- Robin A. C., Reylé C., Derrière S., Picaud S., 2003, *A&A*, 409, 523
- Sale S. E., Magorrian J., 2014, *MNRAS*, 445, 256
- Schönrich R., Asplund M., Casagrande L., 2014, *ApJ*, 786, 7
- Schönrich R., Aumer M., 2017, *MNRAS*, 472, 3979
- Schönrich R., Binney J., Asplund M., 2012, *MNRAS*, 420, 1281
- Schönrich R., McMillan P., Eyer L., 2019, *MNRAS*, 487, 3568
- Sellwood J. A., McGaugh S. S., 2005, *ApJ*, 634, 70
- Sellwood J. A., Trick W. H., Carlberg R. G., Coronado J., Rix H.-W., 2019, *MNRAS*, 484, 3154
- Sivertsson S. et al., 2022, *MNRAS*, 511, 1977
- Sridhar S., Touma J., 1996, *Science*, 271, 973
- Steinmetz M., et al., 2006, *AJ*, 132, 1645
- Syer D., Tremaine S., 1996, *MNRAS*, 282, 223
- Trick W. H., Coronado J., Rix H.-W., 2019, *MNRAS*, 484, 3291
- Vasiliev E., 2019, *MNRAS*, 482, 1525
- Wang J., Hammer F., Yang Y., 2021, *Monthly Notices of the Royal Astronomical Society*, 510, 2242
- Wegg C., Gerhard O., 2013, *MNRAS*, 435, 1874